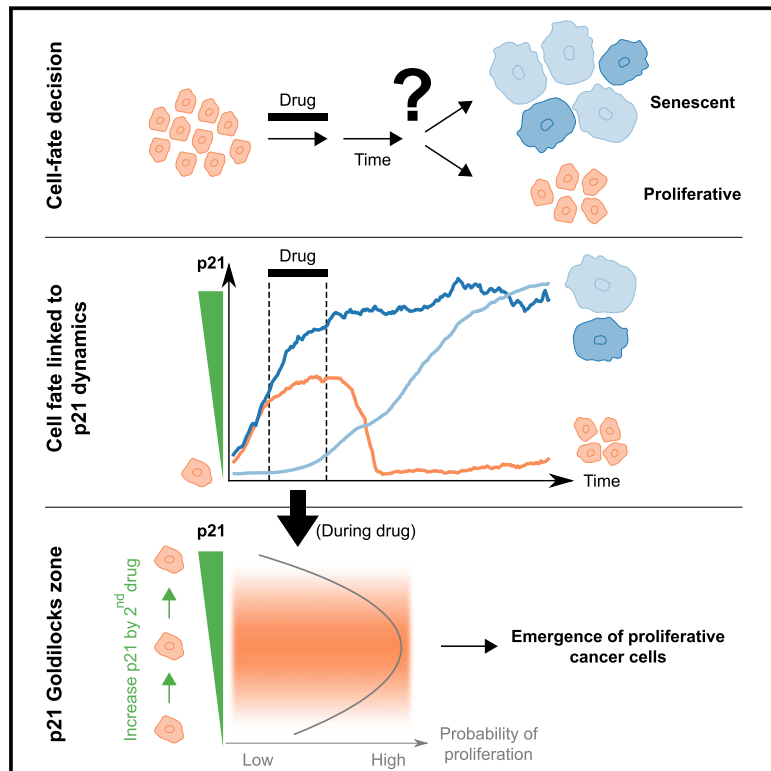# Cell

Patterns of Early p21 Dynamics Determine Proliferation-Senescence Cell Fate after Chemotherapy

Graphical Abstract

Authors

Chien-Hsiang Hsu, Steven J. Altschuler, Lani F. Wu

Correspondence

steven.altschuler@ucsf.edu (S.J.A.), lani.wu@ucsf.edu (L.F.W.)

In Brief

The proliferation-senescence cell-fate decision after drug treatment is determined by three distinct patterns of p21 dynamics. Either a delayed or acute drug-induced p21 response leads to a senescence fate, while an intermediate pulse of p21 response leads to a proliferation fate. This relation between p21 dynamics and cell fate creates a p21 "Goldilocks zone" that favors cell proliferation after drug treatment.

Highlights

- Single-cell tracking unravels heterogeneity in drug-induced senescence decisions

- Different cell fates are reached through three distinct patterns of p21 dynamics

- Most senescence-fated cells have high DNA damage but express low p21 at early times

- A p21 "Goldilocks zone" promotes a proliferation cell fate after treatment

CellPress

Article

Patterns of Early p21 Dynamics Determine Proliferation-Senescence Cell Fate after Chemotherapy

Chien-Hsiang Hsu,[1,2] Steven J. Altschuler,[2,*] and Lani F. Wu[2,3,*]
[1]Simmons Cancer Center, University of Texas Southwestern Medical Center, Dallas, TX 75390, USA
[2]Department of Pharmaceutical Chemistry, University of California, San Francisco, San Francisco, CA 94158, USA
[3]Lead Contact
*Correspondence: steven.altschuler@ucsf.edu (S.J.A.), lani.wu@ucsf.edu (L.F.W.)
https://doi.org/10.1016/j.cell.2019.05.041

SUMMARY

Chemotherapy is designed to induce cell death. However, at non-lethal doses, cancer cells can choose to remain proliferative or become senescent. The slow development of senescence makes studying this decision challenging. Here, by analyzing single-cell p21 dynamics before, during, and days after drug treatment, we link three distinct patterns of early p21 dynamics to final cell fate. Surprisingly, while high p21 expression is classically associated with senescence, we find the opposite at early times during drug treatment: most senescence-fated cells express much lower p21 levels than proliferation-fated cells. We demonstrate that these dynamics lead to a p21 "Goldilocks zone" for proliferation, in which modest increases of p21 expression can lead to an undesirable increase of cancer cell proliferation. Our study identifies a counter-intuitive role for early p21 dynamics in the cell-fate decision and pinpoints a source of proliferative cancer cells that can emerge after exposure to non-lethal doses of chemotherapy.

INTRODUCTION

Cells make fundamental decisions of whether to proliferate or not, and whether to live or die. Much recent progress has been made in understanding the molecular determinants and logic of these decisions at single-cell resolution. Examples include the proliferation-quiescence cell-fate decision under normal conditions (Arora et al., 2017; Barr et al., 2017; Spencer et al., 2013; Yang et al., 2017) and the growth arrest-apoptosis (Paek et al., 2016) and proliferation-apoptosis (Ryl et al., 2017) cell-fate decisions under drug treatment. However, drug-treated cells also have the possibility to choose a senescence fate.

When cancer cells experience non-lethal doses of chemotherapy, such as due to rapid decline of drug concentration during treatment (Gewirtz, 1999), they can withdraw from the cell cycle and enter a senescence-like state, referred to as "therapy-induced senescence" (Ewald et al., 2010). This state is associated with significant changes in morphology and metabolic activities, which are seen when normal cells enter replicative senescence (Kuilman et al., 2010). Clinically, there is growing evidence that therapy-induced senescence occurs in tumors and is associated with improved clinical outcomes (Collado and Serrano, 2010; Haugstetter et al., 2010; Roninson, 2003; Schmitt et al., 2002). Indeed, inducing senescence in cancers has recently been explored as a therapeutic strategy with the potential to reduce cytotoxicity (Ewald et al., 2010; Nardella et al., 2011), engage the immune system (Xue et al., 2007), and potentiate drug combinations (Dörr et al., 2013). However, liabilities of these strategies include that proliferative subpopulations can emerge after treatment (Elmore et al., 2005; Reyes et al., 2018; Roberson et al., 2005) and that senescent cells may have long-term adverse health consequences (Demaria et al., 2017).

A key molecular mediator of therapy-induced senescence is the cyclin-dependent kinase inhibitor p21 (CDKN1A) (Abbas and Dutta, 2009; Cazzalini et al., 2010). p21 halts the cell-cycle progression after transcriptional activation by p53, which is a DNA damage response triggered by many senescence-inducing agents (d'Adda di Fagagna, 2008; Eel-deiry et al., 1993). Paradoxically, there is evidence that p21 has the ability to promote both proliferation and senescence cell-fate outcomes (Abbas and Dutta, 2009; Cazzalini et al., 2010).

On the one hand, classic studies establish an active role of p21 in promoting therapy-induced senescence (Roninson, 2003). p21 accumulates during the process of senescence development (3–7 days) (te Poele et al., 2002), senescent cells are typically observed expressing high levels of p21 (Campisi and d'Adda di Fagagna, 2007), and knockout or overexpression of p21 is sufficient to bypass or induce senescence, respectively (Brown et al., 1997; Fang et al., 1999). However, this body of research has been classically focused on time points after senescence phenotypes have become detectable and has been largely based on pooled-population studies. Recent single-cell work, using live-cell p21 reporters, showed that p21 induction at 5 h after DNA-damaging treatment is predictive of a loss of proliferative potential at 24 h (Stewart-Ornstein and Lahav, 2016). While classic senescence phenotypes have not yet manifested by 24 h after treatment, these results suggest the hypothesis that early, high levels of p21 expression promote a final senescence cell-fate decision.

On the other hand, an emerging body of evidence suggests that p21 plays an active role in promoting a proliferative outcome after

chemotherapy. p21 participates in DNA repair indirectly, by halting cell-cycle progression to provide time for DNA repair and, directly, by regulating the interactions between components involved in repair pathways (Cazzalini et al., 2010). For example, p21 has been shown to enhance the repair of chemotherapy-induced DNA damage and protect glioma cells from apoptosis (Ruan et al., 1998). Additionally, radiation-induced p53-independent up-regulation of p21 in stem cells limited damage accumulation and promoted the expansion of a stem cell pool (Insinga et al., 2013). These results suggest the opposing hypothesis that early, high levels of p21 expression in therapy promote a final proliferation cell fate.

How do early signaling events connect to final proliferation-senescence cell fate? The slow development of senescence phenotypes makes studying this decision at early time points challenging. Classic senescence-associated phenotypes, including morphological changes and senescence-associated β-galactosidase activity (Dimri et al., 1995), are undetectable until multiple days (3–7) after treatment (Ewald et al., 2010). In contrast, early signs of commitment to apoptosis can appear within hours after treatment (Suzuki et al., 2001). Identifying early signaling events that influence cell fate will allow us to understand the logic of the proliferation-senescence decision circuit and, ultimately, inform therapeutic strategies that minimize the emergence of proliferative subpopulations.

Here, we demonstrated a causal role of early p21 dynamics in this decision process. We monitored endogenous p21 dynamics and inferred cell-cycle progression at the single-cell level before, during, and days after drug treatment. p21 was found to promote either proliferation or senescence fates, depending on its patterns of early dynamics during treatment. Surprisingly, during drug treatment, p21 levels were low in S/G2—the cell-cycle phases with highest levels of DNA damage and a major reservoir of senescence-fated cells. Using genetic and pharmacological perturbations, Chk1 activity and proteasomal degradation were identified as molecular mechanisms that repressed p21 expression in the highly damaged cell-cycle phases. A mathematical model was used to elucidate how different patterns of p21 dynamics could emerge from the observed cell-cycle-dependent p21 expression and DNA damage responses. Interestingly, a non-monotonic relationship between p21 expression and cell fate was identified. While either low or high p21 expression during treatment leads to a senescence fate, intermediate p21 levels promote cell proliferation, which leads to a p21 "Goldilocks zone" for proliferation. Finally, studying the relation between cell fate and p21 dynamics enabled the identification and targeting of cells that give rise to the final proliferative subpopulation after treatment. Together, this work revealed opposing functions of early p21 dynamics in determining final cell fate that manifested days after exposure to non-lethal doses of chemotherapy.

RESULTS

1-Day Pulsed Drug Treatment Leads to Mixed Proliferation and Senescence Fates

We developed an experimental system that would drive cancer cells into either proliferation or senescence fates. To induce senescence, we made use of the topoisomerase II inhibitor doxorubicin (Yang et al., 2014), which is one of the most commonly used chemotherapeutic agents and has been shown to induce senescence across multiple cancer cell lines at clinically relevant doses (Chang et al., 1999; Gewirtz, 1999). To have mixed cell fates, a 1-day drug pulse was chosen, motivated by previous studies (Elmore et al., 2005; Roberson et al., 2005) and reported clinical pharmacokinetics (Greene et al., 1983).

A549 non-small cell lung cancer cells were treated with a 1-day pulse of 50 nM doxorubicin (day 1) followed by 4 days without drug (days 2–5). This dosage was low enough that apoptosis was rarely observed yet high enough to be clinically relevant (Gewirtz, 1999). On the final day (day 5), a mixture of senescent and proliferative cellular subpopulations was observed (Figures 1A and 1B, Pulsed). Cells displayed either similar senescence phenotypes as observed after a 5-day sustained treatment (Figure 1A, Pulsed versus Sustained, enlarged morphology and SA-β-gal+) or similar proliferation phenotypes as observed in untreated cells (Figure 1A, Pulsed versus Ctrl). Consistently, expression levels of other senescence or proliferation markers, such as p21, phospho-pRb, and Ki-67, showed bimodal distributions after the pulsed treatment (Figures 1A and 1C, bottom, and S1A), with senescent cells associated with high p21 but low phospho-pRb and Ki-67 expression (Banito and Lowe, 2013; Kuilman et al., 2010). In fact, the mixture of proliferation and senescence fates after 1-day drug pulse was also observed in other chemotherapeutic agents and another cell line (Figure S1B).

What early signaling events might govern the proliferation-senescence cell-fate decision? We focused on the well-established senescence mediator p21 (Abbas and Dutta, 2009; Cazzalini et al., 2010). Previous work showed that drug-induced p21 expression is heterogeneous at 4 h after treatment (Stewart-Ornstein and Lahav, 2016). Consistently, we also found a bimodal distribution of p21 expression at early (12 h) time points during the pulsed treatment (Figure 1C, top), suggesting an early dichotomy of cell-fate decision. Considering the role of p21 in promoting senescence (Campisi and d'Adda di Fagagna, 2007), we hypothesized a simple rule for the proliferation-senescence cell-fate decision (Figure 1C): early low p21 levels stay low and lead to a final proliferation fate, and early high p21 levels stay high and lead to a final senescence fate.

A Live-Cell Reporter System Links Early p21 Expression to Final Cell Fate

Understanding how p21 expression during the drug pulse determines the final proliferation-senescence cell fate requires the ability to: monitor p21 levels at single-cell resolution and link early p21 expression levels to final cell fates. "eFlut" (Stewart-Ornstein and Lahav, 2016), a CRISPR-mediated fluorescence tagging technique, was used to establish a monoclonal A549 cell line with both alleles of p21 endogenously tagged by mVenus, referred to below as A549 p21V (Figures 2A, S2A, and S2B). CFP-tagged H2B and mCherry were also introduced as nuclear and cellular markers, respectively, to facilitate image analysis (Kang et al., 2016). The population doubling time of A549 p21V was less than 1 day (Figure S2C); the average cell-cycle length was 18 h, with 90% of the cells having cell-cycle length less than 24 h (Figure S2D), the duration of our drug pulse.
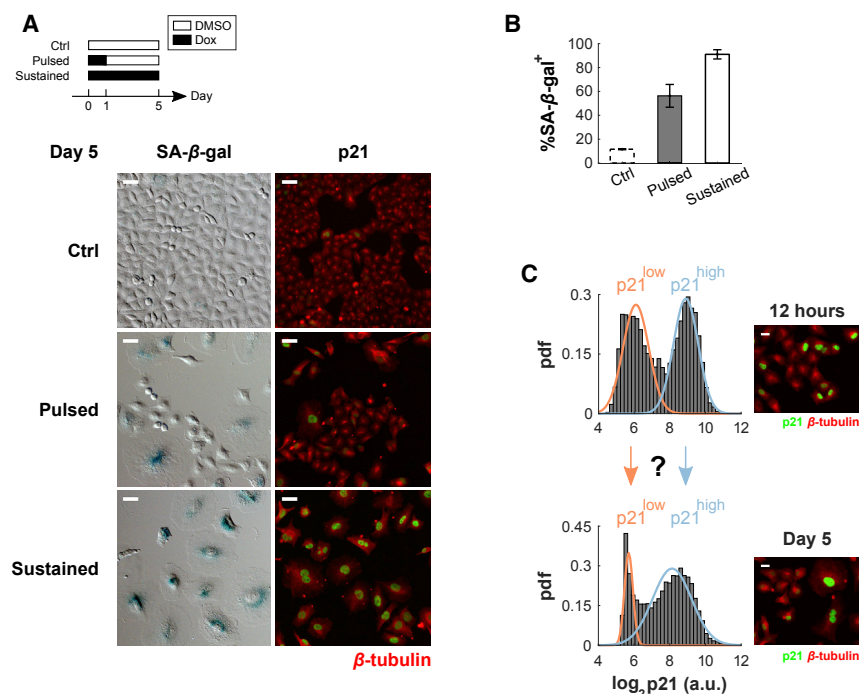
Figure 1. 1-Day Pulsed Drug Treatment Leads to Mixed Proliferation and Senescence Fates

(A) Sample images of A549 cells stained with senescence-associated β-galactosidase (SA-β-gal) or p21 to assess proliferation and senescence states at day 5 after no treatment (Ctrl), pulsed (Pulsed), or continuous (Sustained) doxorubicin treatment (50 nM). Pulsed treatment induced both proliferative and senescent subpopulations. Green channel: p21. Red channel: β-tubulin. Scale bar: 20 μm.

(B) Percentages of cells that showed positive activity of SA-β-gal at day 5 after each treatment scheme. At least 119 cells were examined in each of the three replicate experiments for Ctrl and sustained conditions. At least 94 cells were examined in each of the 24 replicate experiments for pulsed condition. Data are represented as mean ± SEM.

(C) Left: distributions of p21 quantified by immunofluorescence after 12 h of doxorubicin (50 nM) treatment and at day 5 after the pulsed treatment. A Gaussian mixture model was fit to identify the subpopulations with low (orange) or high p21 expression (blue). At least 6,740 cells were quantified at each time point. Right: example images. Green channel: p21. Red channel: β-tubulin. Scale bar: 20 μm.

See also Figure S1.

The levels of p21-mVenus were verified to be highly correlated with the p21 levels measured by fixed-cell immunofluorescence (IF) under both normal and doxorubicin conditions (0.95 and 0.93, respectively; Figure 2B). In addition, the subpopulation of cells with low p21-mVenus levels was enriched for high phospho-pRb levels and vice versa (Figure S2E), which is expected as p21 inhibits cyclin-dependent kinase-mediated phosphorylation of pRb (Figure 2A). Furthermore, after a pulsed doxorubicin treatment, A549 p21V cells showed a mixture of proliferative and senescent subpopulations, similar to what was observed for the untagged parental cells (Figure 2C; senescent cells: high p21 and enlarged nuclei and cell size). Finally, a bimodal distribution of p21-mVenus was observed, as previously noted for both early (12 h) and late (day 4) time points after 1-day pulsed treatment (Figure S2F). (For live-cell experiments, the period after the 1-day drug pulse was reduced to 3 days to improve live-cell microscopy conditions and cell tracking.) Thus, A549 p21V can be used to link early p21 signaling to final cell fate after drug treatment.

The Proliferation-Senescence Cell-Fate Decision Depends on p21 during Pulsed Drug Treatment

We tested for a functional role of p21 in the proliferation-senescence cell-fate decision. As expected at the pooled-population level (Fang et al., 1999; te Poele et al., 2002): p21 expression of A549 p21V increases over time after drug treatment (Figure 2D), and sustained induction of p21 (via nutlin-3a, which stabilizes p53; Tovar et al., 2006), in the absence of DNA damaging drugs, leads to senescence (Figures 2E, S2G, and S2H). Since cells without p21 will choose apoptosis rather than senescence under drug treatment (Han et al., 2002), we hypothesized that inhibiting (or enhancing) p21 expression during the drug pulse

should increase (or decrease, respectively) the fraction of cells with proliferation fates after drug removal (Figure 1C).

We first tested whether decreasing early p21 expression would increase the final proliferative fraction. Small interfering RNA (siRNA) was used to knock down p21 expression for all 5 days ("days 0–5"), only the first day of drug pulse ("days 0–1"), or only after drug removal ("days 1–5") (Figure 2F, left). At day 5, cells were fixed, stained for Ki-67, and imaged to assess the number of proliferative cells (relative to non-targeting [NT] siRNA). Contrary to our hypothesis, inhibiting p21 expression decreased the final fraction of proliferative (Ki-67+) cells (Figure 2F, right; "0–5"). Further, p21 is necessary for final proliferation fates only during—but not after—the drug pulse (Figure 2F, right; "0–1" versus "1–5").

Conversely, we tested whether enhancing p21 expression before the drug pulse would decrease the final proliferative fraction. 1 h of pretreatment with 10 μM nutlin-3a increased p21 expression 2-fold at the end of the 1-day doxorubicin pulse (Figure 2G, left). Unexpectedly, and again contrary to our simple hypothesis, an early increase of p21 expression increased the final fraction of proliferative (Ki-67+) cells by 2.6-fold (Figure 2G, right).

These results (Figures 2F and 2G) demonstrated a functional, time-dependent role of p21 in the proliferation cell-fate decision: p21 induction before or during—but not after—drug pulse is essential for promoting proliferation fate choice. How can the role of p21 in promoting proliferation versus its (well-recognized) function in promoting senescence be reconciled?

In Silico Cell-Cycle Detection Links p21 and Cell-Cycle Dynamics to Cell Fate

To link p21 dynamics to final cell fate at single-cell resolution, we developed the ability to track cells and their progeny
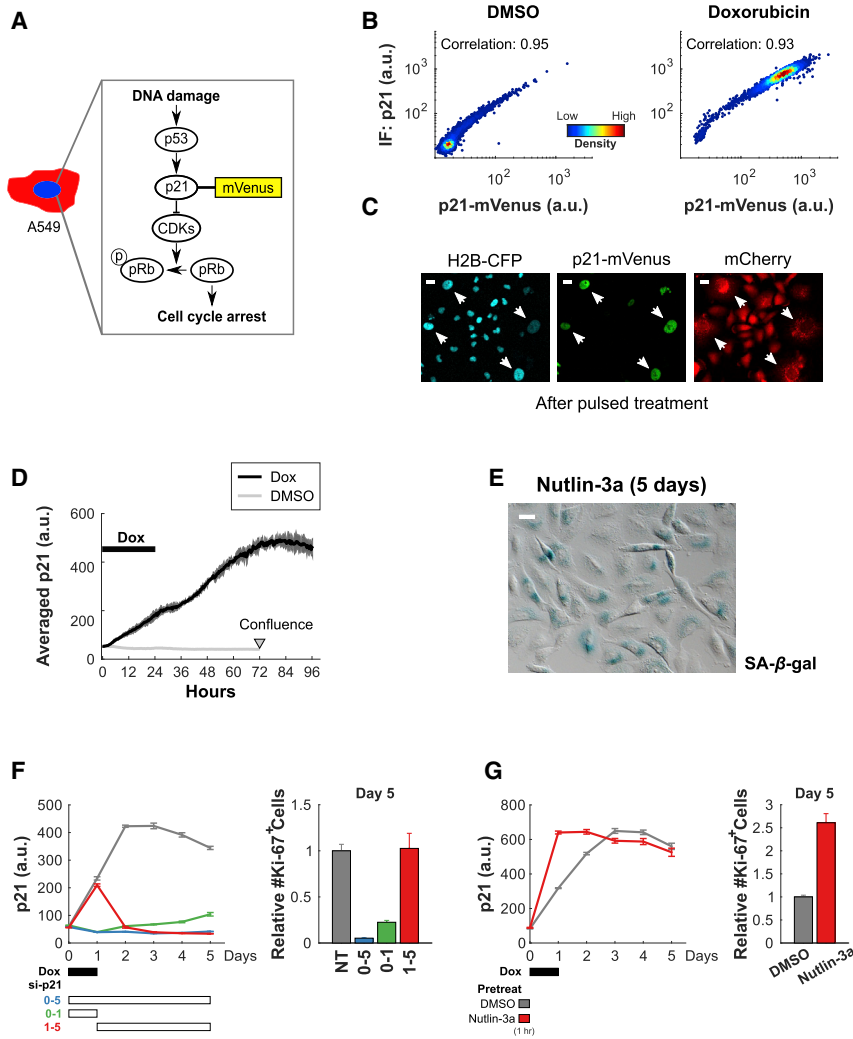
A

DNA damage

p53

p21 → mVenus

CDKs

(p) pRb ← pRb

Cell cycle arrest

A549

B

DMSO

IF: p21 (a.u.)

Correlation: 0.95

10^3

10^2

Low High
Density

10^2 10^3

p21-mVenus (a.u.)

Doxorubicin

Correlation: 0.93

10^3

10^2

10^2 10^3

p21-mVenus (a.u.)

C

H2B-CFP   p21-mVenus   mCherry

After pulsed treatment

D

Averaged p21 (a.u.)

— Dox
— DMSO

600

Dox

400

200

Confluence

0

0 12 24 36 48 60 72 84 96

Hours

E

Nutlin-3a (5 days)

SA-β-gal

F

p21 (a.u.)

500
400
300
200
100
0

0 1 2 3 4 5 Days

Dox
si-p21
0-5
0-1
1-5

Day 5

Relative #Ki-67⁺ Cells

1.5

1

0.5

0

NT 0-5 0-1 1-5

G

p21 (a.u.)

800

600

400

200

0 1 2 3 4 5 Days

Dox
Pretreat
DMSO
Nutlin-3a
(1 hr)

Day 5

Relative #Ki-67⁺ Cells

3
2.5
2
1.5
1
0.5
0

DMSO Nutlin-3a

Figure 2. A Live-Cell Reporter System Links Early p21 Expression to Cell Fate

(A) Simplified network of signal transduction in response to DNA damage. p21 is transcriptionally activated by p53, inhibits cyclin-dependent kinases (CDKs), and causes cell-cycle arrest. p21 reporter cell lines were constructed by endogenously tagging p21 with mVenus at both alleles in a A549 cell line expressing H2B-CFP (blue) as a marker for the nuclear region and mCherry (red) as a marker for the cellular region.

(B) Density scatterplots of immunofluorescence of p21 versus p21-mVenus in single cells under DMSO (left) or after 5 days of 50 nM doxorubicin (right) treatments. At least 3,500 cells were quantified under each condition.

(C) Images of A549 p21V at day 4 after a 1-day pulsed doxorubicin treatment. Both proliferative (small cellular size with low p21 levels) and senescent (enlarged nuclei and cellular area with high p21 levels) subpopulations were observed. Arrowheads: examples of senescent cells. Scale bar: 20 μm.

(D) Averaged p21-mVenus dynamics at the pooled population level in unperturbed condition (DMSO) or after a pulsed 50 nM doxorubicin treatment (Dox). Data are represented as mean (solid lines) ±SD (shaded area).

(E) Senescence-associated β-galactosidase activity in A549 p21V cells after 5 days of sustained 10 μM nutlin-3a treatment. Scale bar: 20 μm.

(F) Genetic perturbation of p21 using siRNA (si-p21). Bottom left: in addition to the pulsed 50 nM doxorubicin treatment (Dox), A549 p21V cells were treated with 25 nM si-p21 either during the entire treatment (days 0–5, blue), just during the drug pulse (days 0–1, green), or after drug removal (days 1–5, red). Non-targeting siRNA (NT) was applied from day 0 to day 5. Cells were fixed, stained for Ki-67, and imaged at day 5. Top left: p21 expression under different schemes of siRNA knockdown. A549 p21V cells were imaged every day to measure p21 levels. Six replicate experiments were performed for each treatment scheme at each time

point. At least 290 cells were quantified in each replicate experiment. Right: relative (to NT) number of Ki-67⁺ cells measured by immunofluorescence at day 5 (6 replicate experiments). Data are represented as mean ± SEM.

(G) Enhanced p21 expression using nutlin-3a. Bottom left: A549 p21V cells were pretreated with DMSO (mock treatment) or 10 μM nutlin-3a for 1 h, followed by the pulsed 50 nM doxorubicin treatment (Dox). Cells were fixed, stained for Ki-67, and imaged at day 5. Top left: effects of nutlin-3a pretreatment on p21 expression. A549 p21V cells were imaged every day to measure p21 levels. Six replicate experiments were performed for each treatment condition at each time point. At least 556 cells were quantified in each replicate experiment. Right: relative (to DMSO) number of Ki-67⁺ cells measured by immunofluorescence at day 5 (6 replicate experiments). Data are represented as mean ± SEM.

See also Figure S2.

accurately across our 5-day experiment (Video S1; STAR Methods). As p21 regulates cell-cycle progression in response to DNA damage (Abbas and Dutta, 2009), an *in silico* cell-cycle phase detector was additionally developed to infer cell-cycle progression. A computational approach to de-mix cell-cycle state in unsynchronized populations was chosen to avoid potential issues introduced by experimental cell synchronization protocols (e.g., altering cell-cycle dynamics, induction of cell stress) (Cooper, 2003; Lanni and Jacks, 1998; Spencer et al., 2013; Uetake and Sluder, 2010). The cell-cycle detector was based on cell-division events and p21 expression, whose levels oscillate predictably across cell-cycle phases in normal growth conditions (Barr

et al., 2017; Starostina and Kipreos, 2012) (Figure S3A, bottom left).

The cell-cycle phase detector consists of three steps (Figure S3A; STAR Methods). First, cell-division events (M phase) were identified from time-lapse videos as the last time point before cytokinesis. Second, S phase intervals were assigned to periods when p21 was at undetectable levels, as p21 is actively degraded during this phase in normal conditions (Nishitani et al., 2008) (Figure S3A, bottom middle). Third, G1 or G2 intervals were assigned to the remaining time points based on their canonical sequential order with M and S events (Figure S3A, bottom right). The main assumption underlying this approach is that p21 levels are undetectable
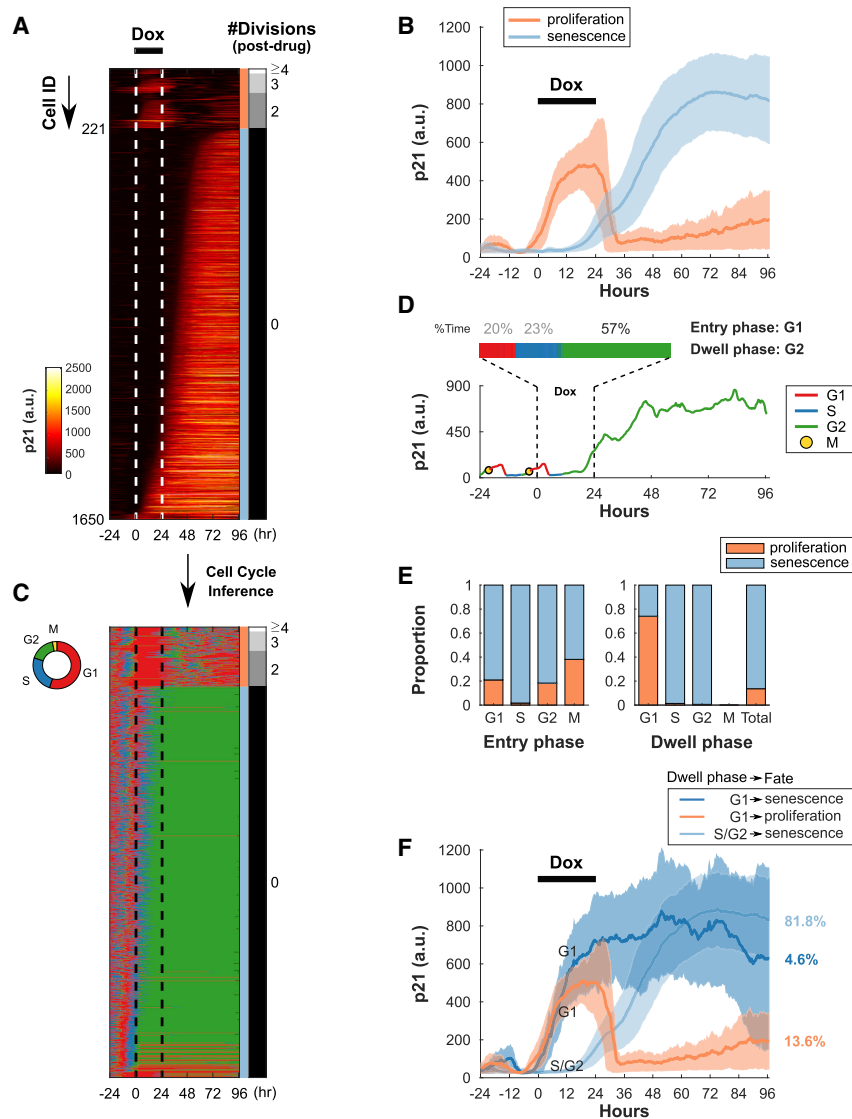
Figure 3. Different Cell-Fate Outcomes Have Different Patterns of p21 Dynamics

(A) Heatmap of p21 dynamics of individual cells (rows, total 1,650 cells) imaged every 20 min starting 24 h before the pulsed doxorubicin (Dox) treatment. Each cell (row) was labeled (at right) by cell fate (orange: proliferation; blue: senescence) and number of divisions after drug removal. Cell fates were defined by the number of divisions after drug removal (proliferation: ≥2 divisions; senescence: 0 divisions). Rows were sorted by number of cell divisions after drug removal followed by p21 induction time.

(B) p21 dynamics of cells grouped by cell fate. Data are represented as median (solid lines) ± median absolute deviation (shaded area). Dox, doxorubicin.

(C) Heatmap of inferred cell-cycle phases. Each row (cell) of p21 dynamics in (A) was converted into cell-cycle phases using the cell-cycle phase detector.

(D) Illustration of entry phase and dwell phase. Cell-cycle progression of an example cell during the drug pulse was enlarged and proportions of time spent in each phase were indicated. This cell had a G2 dwell phase since G2 had the largest time proportion during drug pulse.

(E) Cell-fate distributions of each entry phase (left) and dwell phase (right). No cells with M dwell phase were observed. Total: average across the whole cell population.

(F) p21 dynamics grouped by dwell phase and cell fate. Cells in G1 dwell phase with senescence fates expressed significantly higher p21 during dwell phase than cells in G1 dwell phase with proliferation fates (rank-sum test, p value: 1.5×10^{-4}). Both are significantly higher than cells in S/G2 dwell phase with senescence fates (rank-sum test, p values: 8.9×10^{-50} and 5.3×10^{-124}). Proportions of each group out of the whole population are indicated. Data are represented as median (solid lines) ± median absolute deviation (shaded area). Dox, doxorubicin.

See also Figure S3 and Video S1.

during S phase, which is true under non-drug-treated conditions (Nishitani et al., 2008). To test this assumption in our system, particularly under drug treatment, cells were tracked for 8 h under both unperturbed and perturbed conditions. Cells were then incubated with 5-ethynyl-2′-deoxyuridine (EdU) for 15 min to check whether cells predicted by our detector to be in S phase based on p21 dynamics had, in fact, incorporated EdU (Figures S3B and S3C). These results showed that the cell-cycle phase detector had high accuracy in unperturbed and perturbed conditions (DMSO: 95%; Doxorubicin: 95%, Nutlin-3a: 94%, Figure S3D). Furthermore, the cell-cycle distribution inferred was highly consistent with the distribution inferred using Hoechst staining (Figure S3E) (Belloc et al., 1994).

Thus, our computational approach allowed accurate tracking of individual cells, p21 expression and cell-cycle dynamics across drug treatment, multiple days, and potential cell-division events (Figure S3F).

Different Cell-Fate Outcomes Have Different Patterns of p21 Dynamics

To investigate how early p21 expression during drug pulse determines final cell fate, A549 p21V cells were imaged every 20 min, starting from 24 h before the pulsed doxorubicin treatment (Figure 3A). A cell was defined to have a final proliferation fate if it was able to divide at least twice in the 3 days after drug removal (24–96 h) or to have a final senescence fate if it could not divide even once. (To be confident of the proliferation-fate assignment, cells that divided only once during the 3 days after drug removal [∼10% of all analyzed cells]) were excluded from analysis. In total, the trajectories of 1,650 single-cells were captured: 221 cells with proliferation fates (Figure 3A, orange bar) and 1429 cells with senescence fates (Figure 3A, blue bar).

Cells with different cell fates exhibited distinct p21 dynamics (Figure 3B). Surprisingly, the subpopulation with proliferation fate rapidly induced (median 5.7 h) and maintained high levels of p21 expression during drug pulse, while the subpopulation

with senescence fate had delayed induction (median 36 h) and low p21 expression levels during drug pulse. Though, as might be expected from classic studies of senescence, p21 returned to and was maintained at low levels for the proliferative subpopulation, while p21 rose to and was maintained at high levels for the senescent subpopulation (Figure 3B). Thus, the key signature of cells with proliferation versus senescence fates is pulsed p21 dynamics during drug treatment versus delayed p21 induction. These observations, together with the timed p21 perturbation experiments (Figures 2F and 2G), demonstrated a causal role of early p21 pulse in determining final cell fates.

As p21 regulates cell cycle (Abbas and Dutta, 2009), we next investigated during the drug pulse how p21 dynamics and cell-cycle progression relate to each other and to final fates. The inference of cell-cycle phases revealed distinct patterns of progression for cells with final proliferation versus senescence fates (Figure 3C). Cells with proliferation fates typically had a long G1 phase during the drug pulse and resumed cell cycle after drug removal. In contrast, the majority of cells with senescence fates eventually progressed to a G2 phase during the drug pulse and stayed in G2 after drug removal. To understand cell-cycle progression during drug pulse, two key states were quantified: "entry" and "dwell" phases (Figure 3D). Entry phase was defined to be the cell-cycle phase at treatment onset (0 h), and dwell phase was defined to be the longest cell-cycle phase a cell stayed in during drug pulse (also required to be significantly longer than the maximum observed period for the same phase in untreated conditions; STAR Methods). The terminology "dwell" was used rather than "arrest" as some cells were able to resume cell-cycle progression during drug treatment.

How are entry and dwell phases related to cell fate? Previous studies showed that cells synchronized to different cell-cycle phases before treatment had significantly different responses to chemotherapy (Ling et al., 1996). Analyzing unsynchronized populations with our *in silico* cell-cycle detector, we found that all entry phases except S (known to be highly sensitive to doxorubicin) had sizeable subpopulations with final proliferation fate (Figure 3E, left). In contrast, dwell phase showed a clearer relationship to final cell fate, with only G1 dwell phase having a sizeable proliferative subpopulation (Figure 3E, right). The lack of strong relationship between entry phase and cell fate could be explained by the fact that cells typically did not stay in their entry phases: only 20% of cells had the same dwell phase as their entry phase. Thus, while S entry phase is a good indicator of senescence-fated cells, proliferation-fated cells almost entirely emerge from G1 dwell phase.

How is p21 related to the transition from dwell phase to final fate? Our analysis revealed three distinct patterns of p21 dynamics during drug pulse (Figure 3F). Two p21 patterns led to a senescence fate: either delayed-low (Figure 3F, light blue) or acute-high (Figure 3F, dark blue) p21 responses. In contrast, acute-intermediate p21 responses lead to a proliferation fate (Figure 3F, orange). Thus, p21 can promote opposing proliferation and senescence fates depending on the patterns of its early dynamics.

Drug-Induced p21 Expression Is Repressed by Chk1 and Proteasomal Degradation in S/G2

One of our most puzzling results is that the vast majority of senescence-fated cells had delayed p21 responses in S/G2

phases during drug pulse (Figure 3F, light blue). Doxorubicin is most damaging to cells in S/G2 phases (Potter et al., 2002), and p21 is transcriptionally activated in response to DNA damage (He et al., 2005). Hence, cells in G1 dwell phase would be expected to have lower p21 expression than cells in S/G2 dwell phases, which is the opposite of what we observed (Figure 3F).

To resolve this paradox, we captured the effects of a 1-day doxorubicin treatment on p21 expression and DNA damage (via immunostaining for γH2AX; Mah et al., 2010) using fixed-cell assays across multiple time points. Cell-cycle phase was inferred from Hoechst intensity (STAR Methods). The resulting analysis confirmed that cells in all cell-cycle phases exhibited increased levels of both DNA damage (γH2A.X) and p21 expression after doxorubicin treatment (Figures 4A and S4A). Also, as expected from literature (Abbas and Dutta, 2009), p21 is positively correlated with DNA damage at the population-average level (Figure 4A, Pooled). However, single-cell analysis revealed distinct p21-DNA damage relation in different cell-cycle phases (Figure 4A). Strikingly, although G1 cells had the lowest level of damage, they expressed the highest levels of p21 during treatment: G1 cells had 15-fold and 9-fold higher damage sensitivity (measured by $\Delta p21/\Delta\gamma H2AX$; STAR Methods) than S and G2 cells, respectively (Figures 4A and S4B). Similar trends were observed for other chemotherapeutic agents and another cell line (Figure S4C).

What mechanism prevented higher DNA damage from having higher p21 expression in S/G2 cells? First, p53 was investigated due to its role as the direct transcriptional activator of p21 and key transducer of DNA damage signals (Bieging et al., 2014). Specifically, we tested whether low p21 expression in S/G2 was due to low p53 expression. Consistent with the function of p53 on p21 transcription, knockdown of p53 by siRNA reduced doxorubicin-induced p21 expression to untreated (DMSO) levels (Figure S4D). However, p53 was considerably higher in S/G2 cells than G1 cells at 12 and 24 h of doxorubicin treatment, which is opposite to the trend for p21 (Figure 4B) but consistent with cell-cycle-dependent levels of DNA damage. Hence, the low levels of p21 expression in the phases with the highest levels of damage (S/G2) could not be simply explained by p53 levels alone.

Second, Myc was investigated due to its reported ability to suppresses p53-mediated transcriptional activation of p21 in response to DNA damage (Seoane et al., 2002) (Figure 4C). Knockdown of Myc by siRNA under doxorubicin treatment resulted in relatively similar (1.4- and 1.6-fold) increases of damage sensitivity for both G1 and G2 cells, respectively (Figure 4D), suggesting that Myc is unlikely to account for the observed cell-cycle-dependent differential activation of p21.

Third, the role of proteasomal degradation of p21 was investigated (Figure 4C), as proteasome-mediated p21 degradation was suggested to be cell-cycle dependent (Bashir et al., 2004; Starostina and Kipreos, 2012; Wei et al., 2004). Inhibition of the proteasome pathway by bortezomib differentially affected the damage sensitivity of G1 and S/G2 cells (Figure 4E). Under doxorubicin treatment, bortezomib increased the damage sensitivity of S and G2 cells to 6- and 3-fold, respectively, but modestly decreased the damage sensitivity of G1 cells by 28%. Thus,
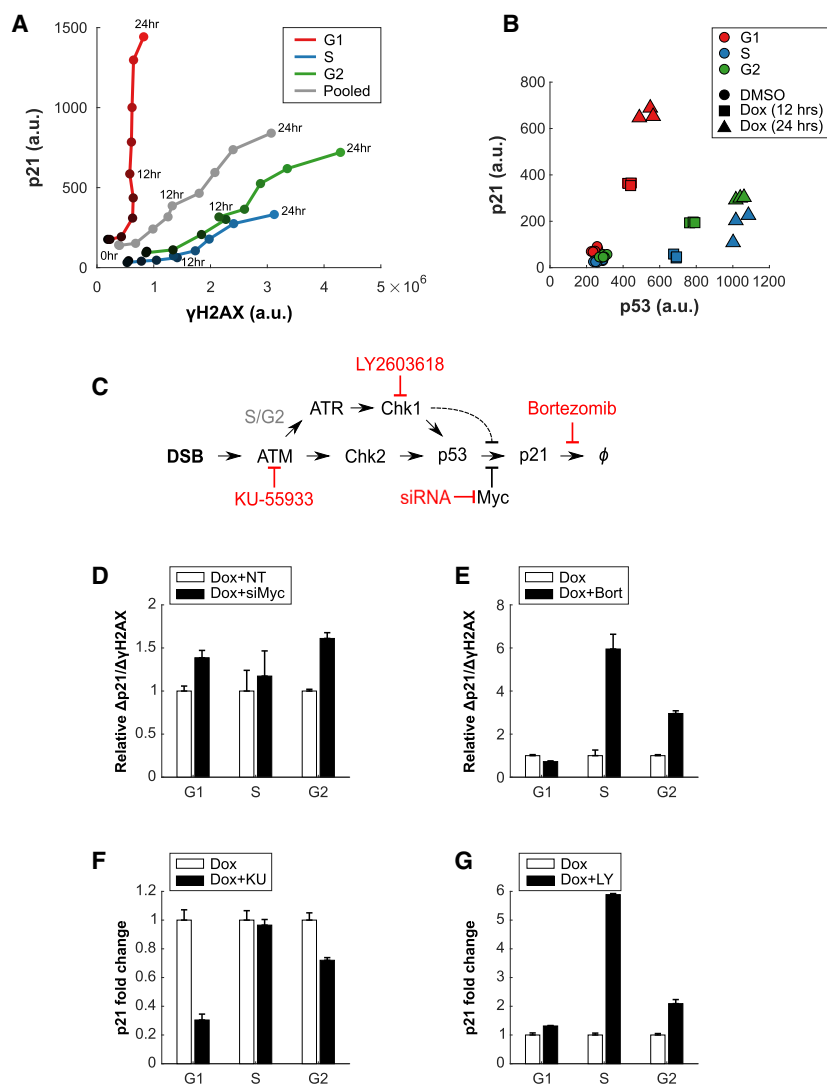
Figure 4. Drug-Induced p21 Expression Is Repressed by Chk1 and Proteasomal Degradation in S/G2

(A) Time course of p21 versus DNA damage grouped by cell-cycle phases. A549 p21V cells were treated with 50 nM doxorubicin and fixed and stained for γH2A.X at the multiple time points (0, 1, 3, 6, 9, 12, 15, 18, 21, and 24 h). Cell cycle was inferred using Hoechst intensity. γH2A.X was quantified in single cells by total immunofluorescent intensity in each nuclear region. p21 was measured in single cells by average mVenus intensity in each nuclear region. Population average of p21 is shown against population average of γH2A.X at each time point. Damage sensitivities of each cell-cycle phase were estimated by slopes of linear regression models. Slopes for G1, S, and G2 were 1.8×10^{-3}, 1.2×10^{-4}, and 2×10^{-4} (a.u.), respectively. At least 900 cells were quantified for each cell-cycle phase at each time point.

(B) Scatterplot of p21 versus p53 expression grouped by cell-cycle phases. Cells were treated with DMSO (control) or 50 nM doxorubicin and then fixed and stained for p53 at 12 or 24 h. p21 and p53 were quantified by average mVenus and immunofluorescent intensity, respectively, in each nuclear region. The population average is reported. Data shown are three replicate experiments for each condition and time point. For each replicate experiment, at least 159 cells were quantified for each cell-cycle phase.

(C) Network diagram of DNA-damage response and regulation of p21 expression. Pharmacological and genetic perturbations used in (D)–(G) are shown in red. DSB, double-strand break.

(D) Relative damage sensitivity (Δp21/ΔγH2A.X) under Myc knockdown. Cells were treated with 50 nM doxorubicin (Dox) together with 25 nM siRNA targeting Myc (siMyc) or non-targeting siRNA (NT) for 12 h. Cells were then fixed and stained for γH2A.X. Damage sensitivity (Δp21/ΔγH2A.X) was quantified by the slope of a linear regression model that captures the increased expression of p21 (Δp21, compared to p21 levels in untreated conditions) relative to the increased amount of DNA damage (ΔγH2A.X, compared to γH2A.X levels in untreated conditions). Six replicate experiments were performed for each condition. At least 220 cells were quantified for each cell-cycle phase in each replicate experiment. Data were normalized to Dox+NT treatment and are represented as mean ± SEM.

(E) Relative damage sensitivity (Δp21/ΔγH2A.X) under proteasome inhibition. Cells were treated with 50 nM doxorubicin (Dox) together with 40 nM bortezomib (Bort) to inhibit proteasome pathways for 12 h. Cells were fixed and stained for γH2A.X. Damage sensitivity was quantified as (D). Six replicate experiments were performed for each condition. At least 235 cells were quantified for each cell-cycle phase in each replicate experiment. Data were normalized to doxorubicin-only treatment and are represented as mean ± SEM.

(F and G) Effects of inhibiting ATM (F) and Chk1 (G) on p21 expression in response to DNA damage in different cell-cycle phases. Cells were treated with 50 nM doxorubicin (Dox) together with 10 μM ATM inhibitor KU-55933 (KU) or 5 μM Chk1 inhibitor LY2603618 (LY) and were fixed at 12 h. Cell-cycle phase was inferred using Hoechst intensity, and p21 was quantified as (A). Three replicate experiments were performed for each condition. At least 231 cells were quantified for each cell-cycle phase in each replicate experiment. Data were normalized to doxorubicin-only treatment and are represented as mean ± SEM.

See also Figure S4.

proteasomal degradation of p21 plays a role in the differential activation of p21 at different phases of the cell cycle.

Finally, components of the DNA-damage response pathway were investigated for their abilities to alter drug-induced p21 expression in a cell-cycle-dependent manner (Figure 4C). Ataxia-telangiectasia mutated (ATM) is the main signal transducer of DNA double-strand breaks (DSBs), leading to stabilized p53 and induced p21 expression (Kurz et al., 2004; Smith et al., 2010). During S and G2 phases, ATR/Chk1 signaling is activated by resected DSBs, contributing to intra-S and G2/M checkpoints by stabilizing p53 and inducing p21 (Maréchal and Zou, 2013; Shiotani and Zou, 2009; Taylor and Stark, 2001); though, it has also been reported that Chk1 can inhibit p21 expression (Beckerman et al., 2009).

To evaluate the roles of ATM and Chk1, cells were co-treated with doxorubicin and either an inhibitor of ATM (10 μM KU-55933) or Chk1 (5 μM LY2603618) for 12 h (Hickson et al., 2004; King et al., 2014). The results showed that ATM and
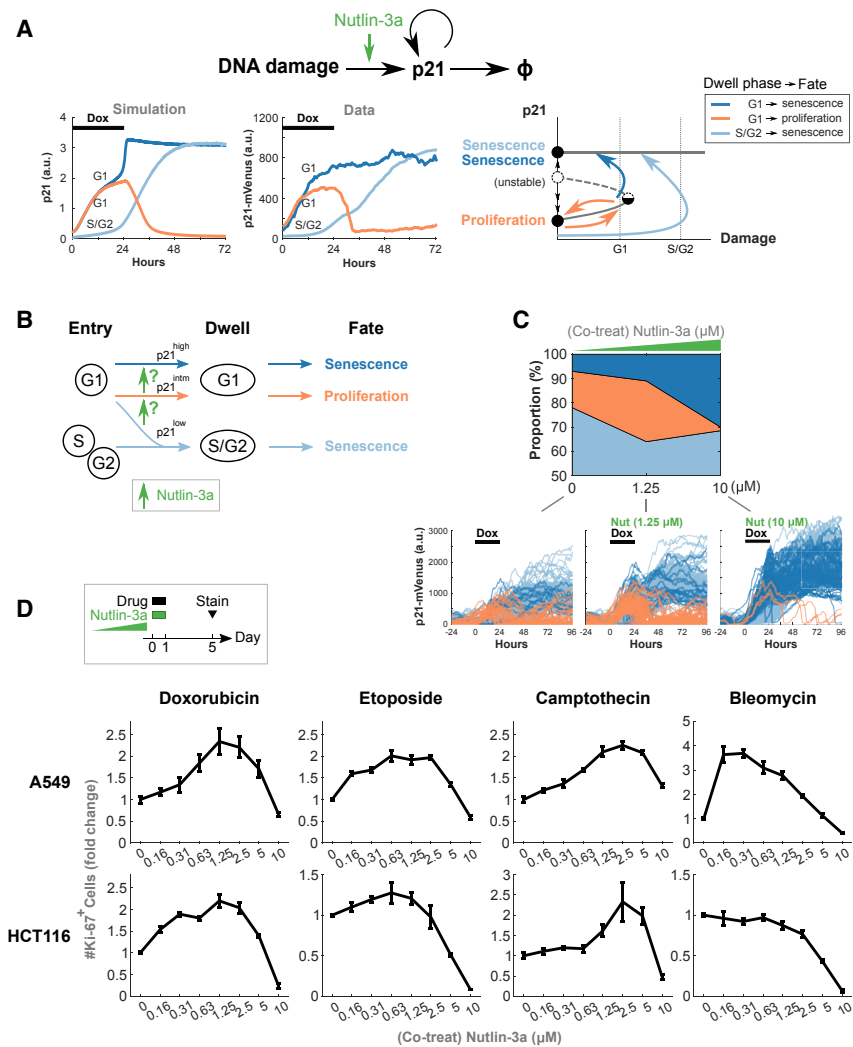
Figure 5. A p21 "Goldilocks Zone" Promotes the Proliferative Cell Fate after Chemotherapy

(A) Top: a conceptual model of p21 dynamics in response to DNA damage. Bottom left: simulated (Simulation) and observed (Data) p21 dynamics (median of each subpopulation shown). Right: cartoon of phase plane diagram relating dynamics of p21 and DNA damage.

(B) Flux view of the cell-fate decision process: from entry to dwell phase (See Figure 3D) to final cell fate. Enhanced p21 induction, e.g., via nutlin-3a, is hypothesized to change the flux from p21^{low} to p21^{intm} to p21^{high} (green arrows and question marks). Intm, intermediate.

(C) Changes of flux through the cell-fate decision process by nutlin-3a co-treatment. Cells were co-treated with nutlin-3a at 0 μM (without co-treatment), 1.25 μM or 10 μM under 1-day pulsed doxorubicin (50 nM) treatment. Cells were imaged and tracked every 20 min for 5 days starting from 24 h before the pulsed treatment. Top: percentage of each dwell-phase-cell-fate subpopulation. Color legends are shared with (A) and (B). Bottom: p21 dynamics of individual cells colored by dwell phase and cell fate. Random samples of 200 single-cell p21 dynamics were shown for each condition. Total cell trajectories are 256, 396, and 739 for 0, 1.25, and 10 μM nutlin-3a co-treatment conditions, respectively. Dox, doxorubicin; Nut, nutlin-3a.

(D) Generality of the p21 "Goldilocks zone" across multiple chemotherapeutic agents and two cell lines. Top: illustration of the experimental design. Cells were treated with a 1-day pulse of drug together with different doses of nutlin-3a, followed by 4 days in drug-free media. Cells were fixed, stained for Ki-67, and imaged at day 5. Bottom: relative number of Ki-67$^+$ cells at different doses of co-treated nutlin-3a. Three replicate experiments were performed for each condition. Data were normalized to drug-only (0 μM nutlin-3a) treatment and are represented as mean ± SEM.

See also Figure S5 and Table S1.

Chk1 differentially regulated drug-induced p21 expression in different cell-cycle phases. Inhibition of ATM by KU-55933 reduced p21 expression by 70% for G1 cells but had no effect for cells in S phase and only modestly decreased p21 levels (by 28%) for G2 cells (Figure 4F). In contrast, inhibition of Chk1 by LY2603618 significantly increased p21 expression for S and G2 cells (6- and 2-fold, respectively) but only modestly increased p21 expression for G1 cells (1.3-fold) (Figure 4G). These data suggested that high p21 expression during G1 was due mainly to activation by ATM signaling, whereas low p21 expression for S and G2 was due mainly to repression by Chk1 signaling.

Together, these results showed that ATM signaling is required for high levels of drug-induced p21 expression in G1, while the unexpectedly lower levels of p21 expression in S/G2 is due to repression by the Chk1 signaling and proteasomal degradation. These results suggested molecular mechanisms by which cells in S/G2 phases—the cell-cycle phases most damaged by doxorubicin and a major reservoir for senescence-fated cells—had the lowest levels of p21 expression during drug treatment.

A Mathematical Framework for Understanding the Emergence of Different Patterns of p21 Dynamics

To understand how different patterns of p21 dynamics could emerge, we adapted a previous mathematical model of p21 signaling dynamics (Overton et al., 2014) (Figure 5A, top; STAR Methods). The model incorporated three essential processes: cell-cycle-dependent DNA damage (Figure S5A), positive feedback of p21 (Figure S5B) (Passos et al., 2010), and cell-cycle-dependent p21 degradation (Figure S5C). The model largely captured the observed p21 dynamics (Figure 5A, left) and suggested possible mechanisms underlying the three observed patterns of p21 dynamics with the two cell-fate outcomes. The model revealed a bistability of p21 states—corresponding to proliferation (p21^{low} state) and senescence (p21^{high} state) fates—and the capacity for the system to undergo a saddle-node bifurcation during drug treatment (Figure 5A, right).

At intermediate levels of DNA damage (as observed in G1 phase), proliferation and senescence fates could emerge due to stochastic differences in p21 expression. If p21 levels remained

below the unstable state (Figure 5A, right, dashed gray curves) during treatment, cells would return to the p21^{low} state and have proliferation fates after drug removal (Figure 5A, right, orange); otherwise, cells would move to the p21^{high} state and have a senescence fate (Figure 5A, right, dark blue). In contrast, high levels of DNA damage (as observed in S/G2 phases) pushed the system beyond the bifurcation point, leaving only a single, p21^{high} steady state (Figure 5A, right). However, due to strong degradation, p21 levels in S/G2 remained low until DNA damage reached high enough levels (Figure 5A, right, light blue). Thus, the model provided a unifying framework to link p21 dynamics, cell-cycle-dependent differences in p21 degradation and DNA damage, and final cell fate.

A p21 "Goldilocks Zone" Promotes the Proliferative Cell Fate after Chemotherapy

A natural idea to reduce the emergent proliferative cancer cells after chemotherapy would be to increase p21 levels, as high sustained p21 leads to senescence (Fang et al., 1999). However, our study of early p21 dynamics and cell fate suggests an interesting hypothesis—increasing p21 levels during the drug pulse would lead to a non-monotonic change in the final proliferative outcomes (Figure 5B). An initial increase in p21 induction would shift cells from having senescence to proliferation fates by preventing transition of G1-entry cells to S/G2 (Figure 5B, bottom green arrow); however, further increasing p21 expression would shift cells from having proliferation back to senescence fates by facilitating G1 dwell-phase cells to transit from a p21^{intm} to a p21^{high} state (Figure 5B, top green arrow; Figure 5A, orange to dark blue curves). Thus, increasing p21 levels would be predicted to create a "Goldilocks zone" for proliferation as cells shift from low (senescence fate), to intermediate (proliferation fate), to high (senescence fate) p21 subpopulations (Figure 5B).

To test this hypothesis, nutlin-3a was used to enhance p21 expression without introducing additional DNA damage (Figures S2G and S2H). Individual cells were co-treated with nutlin-3a (0, 1.25, or 10 μM) and tracked during the doxorubicin pulse treatment (Figure 5C, bottom). Consistent with the prediction, our analysis showed that enhancing p21 expression first increased the fraction of subpopulations with intermediate p21 levels (G1 → proliferation fate), and then redirected cells to high p21 expression (G1 → senescence fate). As a consequence, the final proliferation cell-fate outcomes first increased and then decreased as nultlin-3a concentration increased (Figure 5C, top).

The generality of p21 "Goldilocks zone" was further tested using other chemotherapeutic agents and cell lines (Figures 5D and S5D). Cells were co-treated with increasing doses of nutlin-3a during the drug pulse, fixed, stained for Ki-67, and imaged at day 5 to assess the number of proliferative cells (Figure 5D, schema). The result showed that the number of Ki-67^{+} cells reached a maximum at intermediate concentrations of co-treated nutlin-3a before decreasing at the highest concentration. This suggests that a p21 "Goldilocks zone" for proliferation cell-fate outcomes may be a general phenomenon.

Strategies for Reducing the Proliferative or Senescent Subpopulations

What strategies could reduce the proliferative subpopulation of cells that emerge after pulsed treatment? Targeting DNA dam-

age checkpoints has been shown to offer promising opportunities in combination with chemotherapy (O'Connor, 2015). Our analysis pinpointed the major source of the final proliferative population as G1-dwell cells (Figures 3F and 6A), suggesting the importance of G1/S checkpoint for cells to have a proliferation fate. Thus, we hypothesized that targeting the G1/S checkpoint during chemotherapy could be more effective in reducing final proliferative subpopulation than targeting the G2/M checkpoint.

Consistent with this hypothesis, abrogating the G1/S checkpoint (e.g., by inhibiting ATM via KU-55933) was more effective than abrogating the G2/M checkpoint (e.g., by inhibiting Chk1 via LY2603618 at reducing the number of proliferative cells at day 5 after 1-day pulsed treatments of doxorubicin (topoisomerase II inhibitor) and bleomycin (radiomimetic) (Figure 6B). In contrast, only a small fraction of cells activated the G1/S checkpoint during camptothecin (topoisomerase I inhibitor) treatment (Figure S6), and abrogating the G1/S checkpoint was not as effective (Figure 6B) (Xiao et al., 2006). While ATM has also been reported to contribute to the G2/M checkpoint, a checkpoint arrest in G2 does not absolutely depend on ATM (Shaltiel et al., 2015), consistent with the observation that inhibiting ATM mainly affected the G1 subpopulation in our system (Figure 4F). Together, these results highlight the importance of targeting the G1/S checkpoint for eliminating emergent proliferative cells after chemotherapy.

Finally, we explored strategies to reduce the remaining senescent subpopulations after pulsed treatment, as they may have long-term adverse consequences (Demaria et al., 2017). In particular, we investigated whether one or both of the senescent subpopulations (Figures 3F and 6A, dark and light blue curves) can be eliminated by senolytic drugs. Proliferative and senescent subpopulations were treated with Navitoclax, an inhibitor of anti-apoptotic proteins that selectively kills senescent cells (Chang et al., 2016). The results showed that more than 90% of the cells in both senescent subpopulations can be effectively eliminated by this drug (Figure 6C). Taken together, our study suggests the hypothesis that abrogating the G1/S checkpoint during treatment could reduce the final proliferative subpopulation and that application of senolytic drugs after treatment could reduce the remaining senescent subpopulation.

DISCUSSION

Chemotherapy is designed to induce cell death. However, cancer cells can experience non-lethal doses due to unavoidable, rapid declines in drug concentration (Gewirtz, 1999). In these non-lethal ranges, cells can choose to either remain proliferative or become senescent. How is this decision made and what are the design principles underlying this decision? To address these questions, we disentangled heterogeneity across p21 dynamics, cell-cycle progression, and DNA damage at early times after treatment and linked them to final cell fate that manifested days later.

Our longitudinal single-cell analysis revealed three distinct patterns of early p21 dynamics: one pattern leading to proliferation and two other patterns leading to senescence fates days
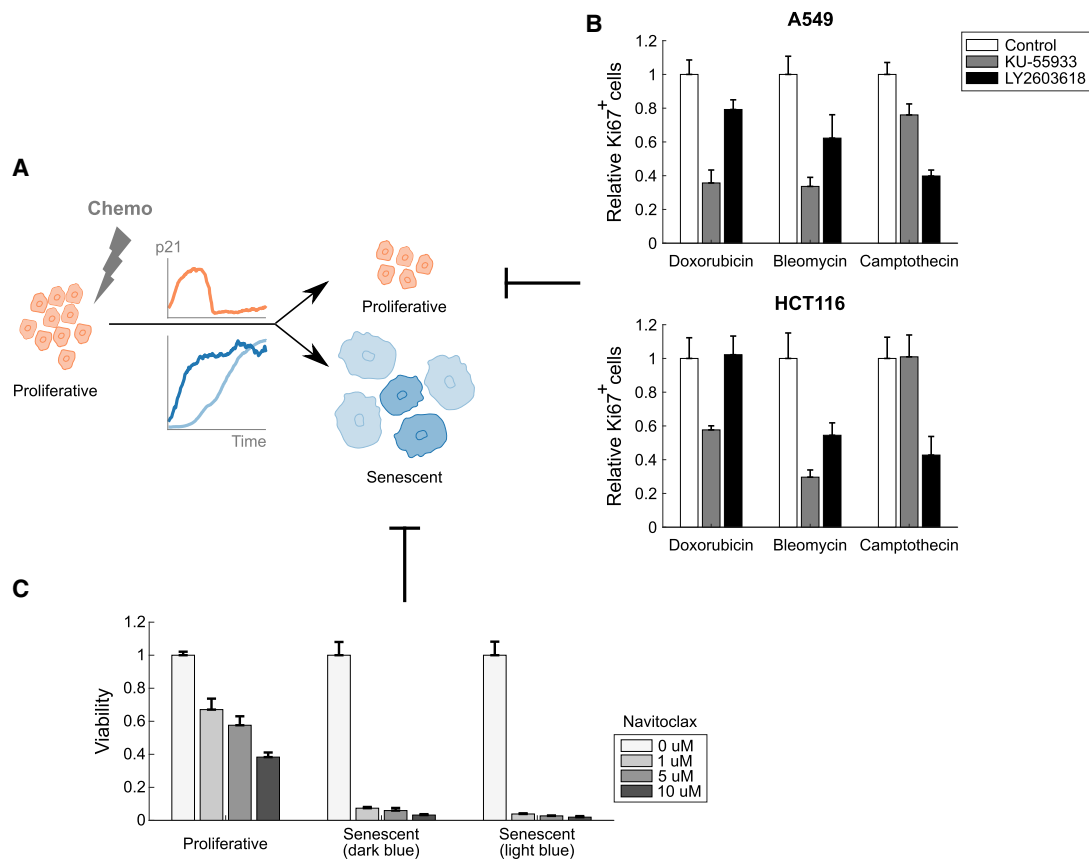
Figure 6. Strategies for Reducing the Proliferative or Senescent Subpopulations

(A) Summary of the source of proliferative and senescent populations after a pulsed treatment of chemotherapy. Cell subpopulations and p21 dynamics colored as in Figure 3F.

(B) Effect on proliferative cell fate after combination of chemotherapy and G1/S or G2/M checkpoint inhibitor. A549 p21V and HCT116 cells were treated with different chemotherapeutic agents together with 10 μM KU-55933 or 5 μM LY2603618 for 24 h followed by 4 days in drug-free media. Cells were then fixed and stained for Ki-67 at day 5. Data were normalized to chemotherapeutic agent-only treatment (Control) and are represented as mean ± SEM (n = 5).

(C) Effects of senolytic drug on distinct senescent subpopulations. Populations of A549 p21V cells, enriched for the two different senescent subpopulations (Figure 3F), were prepared by 5-day sustained treatments of nutlin-3a (dark blue) or doxorubicin (light blue) followed by 24 h of Navitoclax (ABT-263) treatment. Data are represented as mean ± SEM (n = 3).

after drug removal (Figure 3F). These patterns of early dynamics were missed from pooled-population studies, where the senescence decision is simply associated with high p21 expression (Figure 1) (Kuilman et al., 2010). Unexpectedly, during drug treatment most senescence-fated cells expressed low levels of p21, despite experiencing high DNA damage, and only a small portion of senescence-fated cells expressed high levels of p21. In contrast, proliferation-fated cells expressed intermediate levels of p21 and returned to low p21-expressing state after drug removal. The emergence of these distinct patterns of p21 dynamics was recapitulated by a mathematical model, which related p21 and DNA damage levels (Figure 5A). Below intermediate levels of drug-induced DNA damage (e.g., G1 cells), cells can either stay in a $p21^{low}$ state (proliferation) or be driven by noise to a final $p21^{high}$ state (senescence), reflecting an underlying bistability modeled by the system. In contrast, at high levels of drug-induced DNA damage (e.g., S/G2 cells), only a final $p21^{high}$ state (senescence) exists. The heterogeneity

of cell-fate outcomes driven by a combination of stochasticity and switch-like behavior is also observed in other cell-fate decision circuits (Kwon et al., 2017; Reyes et al., 2018; Spencer et al., 2013).

The relation between the patterns of p21 dynamics and cell fates led to a non-monotonic response to increasing p21 stimulus, a phenomenon similar to a previously reported non-monotonic apoptosis response to increasing c-Jun N-terminal kinase (JNK) signaling (Janes et al., 2005). Specifically, while both inhibiting (Figures 2F) and strongly enhancing p21 expression (Figures 5D and S5D) during treatment decreased proliferative outcomes, we found a p21 "Goldilocks zone" that actually increased the final fraction of proliferative cells. This result suggested that current strategies for increasing p53 (and thus p21) activity during chemotherapy (Burgess et al., 2016) could have undesirable consequences of increasing the number of proliferative cancer cells when drug concentrations (inevitably) decline.

Our study raises the question of why drug-induced p21 expression is particularly repressed in the most damaged cell-cycle phases (Figure 4). One possibility is that this prevents spurious p21 induction in response to mild DNA damage levels in S and G2 phases—where cells typically experience higher endogenous DNA damage caused by DNA replication and topological stress (Branzei and Foiani, 2008)—which could lead to a permanent cell-cycle arrest (Krenning et al., 2014; Shaltiel et al., 2015). The inhibitory regulation of p21 expression in S/G2 we observed would serve to increase the DNA damage threshold for activating p21 response, so that only cells with severe DNA damage would withdraw from the cell cycle. It is unknown whether other p21 regulation mechanisms, such as miRNA and p21 phosphorylation (Jung et al., 2010), are also involved in shaping the p21 induction threshold across cell cycle.

The principle underlying the proliferation-senescence cell-fate decision process illustrated by our work provides a starting point for addressing many interesting questions. In particular, how does this p21-driven decision process interact with other senescence pathways, including p16-pRb driven senescence (Rayess et al., 2012)? How do different senescence pathways interact to maintain the long-term cell-cycle arrest (Passos et al., 2010; Reinhardt et al., 2010; Reyes et al., 2018)? Answers to these questions will help elucidate fundamental design properties of cell-fate decision processes triggered by therapy and guide strategies for biasing cell fate toward clinically desired outcomes.

STAR★METHODS

Detailed methods are provided in the online version of this paper and include the following:

- KEY RESOURCES TABLE
- LEAD CONTACT AND MATERIALS AVAILABILITY
- EXPERIMENTAL MODEL AND SUBJECT DETAILS
    - Cell Culture
- METHOD DETAILS
    - Drug Treatment
    - Cell Line Construction
    - Senescence-Associated β-galactosidase Assay
    - Immunofluorescence
    - siRNA Transfection
    - EdU Assay
    - Image Acquisition
- QUANTIFICATION AND STATISTICAL ANALYSIS
    - Image Analysis and Cell Tracking
    - *In Silico* Cell-Cycle Inference
    - Quantification of EdU Intensity
    - Definition of p21 Induction
    - Definition of Dwell Phase
    - Comparison of p21 Expression during Dwell Phase between Cellular Subpopulations
    - Inference of Cell-Cycle Phase using Hoechst Intensity
    - Quantification of DNA-Damage Sensitivity ($\Delta p21/\Delta\gamma H2A.X$)
    - Definition of Ki-67$^+$ Cells
    - Mathematical Model of p21 Dynamics
- DATA AND CODE AVAILABILITY

REFERENCES

Abbas, T., and Dutta, A. (2009). p21 in cancer: intricate networks and multiple activities. Nat. Rev. Cancer *9*, 400–414.

Arora, M., Moser, J., Phadke, H., Basha, A.A., and Spencer, S.L. (2017). Endogenous Replication Stress in Mother Cells Leads to Quiescence of Daughter Cells. Cell Rep. *19*, 1351–1364.

Banito, A., and Lowe, S.W. (2013). A new development in senescence. Cell *155*, 977–978.

Barr, A.R., Cooper, S., Heldt, F.S., Butera, F., Stoy, H., Mansfeld, J., Novák, B., and Bakal, C. (2017). DNA damage during S-phase mediates the proliferation-quiescence decision in the subsequent G1 via p21 expression. Nat. Commun. *8*, 14728.

Bashir, T., Dorrello, N.V., Amador, V., Guardavaccaro, D., and Pagano, M. (2004). Control of the SCF(Skp2-Cks1) ubiquitin ligase by the APC/C(Cdh1) ubiquitin ligase. Nature *428*, 190–193.

Beckerman, R., Donner, A.J., Mattia, M., Peart, M.J., Manley, J.L., Espinosa, J.M., and Prives, C. (2009). A role for Chk1 in blocking transcriptional elongation of p21 RNA during the S-phase checkpoint. Genes Dev. *23*, 1364–1377.

Belloc, F., Dumain, P., Boisseau, M.R., Jalloustre, C., Reiffers, J., Bernard, P., and Lacombe, F. (1994). A flow cytometric method using Hoechst 33342 and propidium iodide for simultaneous cell cycle analysis and apoptosis determination in unfixed cells. Cytometry *17*, 59–65.

Bieging, K.T., Mello, S.S., and Attardi, L.D. (2014). Unravelling mechanisms of p53-mediated tumour suppression. Nat. Rev. Cancer *14*, 359–370.

Bise, R., Yin, Z.Z., and Kanade, T. (2011). Reliable cell tracking by global data association. In Proceedings of the IEEE International Symposium on Biomedical Imaging: From Nano to Macro (IEEE), pp. 1004–1010.

Branzei, D., and Foiani, M. (2008). Regulation of DNA repair throughout the cell cycle. Nat. Rev. Mol. Cell Biol. *9*, 297–308.

Brown, J.P., Wei, W., and Sedivy, J.M. (1997). Bypass of senescence after disruption of p21CIP1/WAF1 gene in normal diploid human fibroblasts. Science 277, 831–834.

Burgess, A., Chia, K.M., Haupt, S., Thomas, D., Haupt, Y., and Lim, E. (2016). Clinical Overview of MDM2/X-Targeted Therapies. Front. Oncol. 6, 7.

Campisi, J., and d'Adda di Fagagna, F. (2007). Cellular senescence: when bad things happen to good cells. Nat. Rev. Mol. Cell Biol. 8, 729–740.

Cazzalini, O., Scovassi, A.I., Savio, M., Stivala, L.A., and Prosperi, E. (2010). Multiple roles of the cell cycle inhibitor p21(CDKN1A) in the DNA damage response. Mutat. Res. 704, 12–20.

Chang, B.D., Broude, E.V., Dokmanovic, M., Zhu, H., Ruth, A., Xuan, Y., Kandel, E.S., Lausch, E., Christov, K., and Roninson, I.B. (1999). A senescence-like phenotype distinguishes tumor cells that undergo terminal proliferation arrest after exposure to anticancer agents. Cancer Res. 59, 3761–3767.

Chang, J., Wang, Y., Shao, L., Laberge, R.M., Demaria, M., Campisi, J., Janakiraman, K., Sharpless, N.E., Ding, S., Feng, W., et al. (2016). Clearance of senescent cells by ABT263 rejuvenates aged hematopoietic stem cells in mice. Nat. Med. 22, 78–83.

Collado, M., and Serrano, M. (2010). Senescence in tumours: evidence from mice and humans. Nat. Rev. Cancer 10, 51–57.

Cooper, S. (2003). Rethinking synchronization of mammalian cells for cell cycle analysis. Cell. Mol. Life Sci. 60, 1099–1106.

d'Adda di Fagagna, F. (2008). Living on a break: cellular senescence as a DNA-damage response. Nat. Rev. Cancer 8, 512–522.

Demaria, M., O'Leary, M.N., Chang, J., Shao, L., Liu, S., Alimirah, F., Koenig, K., Le, C., Mitin, N., Deal, A.M., et al. (2017). Cellular Senescence Promotes Adverse Effects of Chemotherapy and Cancer Relapse. Cancer Discov. 7, 165–176.

Dimri, G.P., Lee, X., Basile, G., Acosta, M., Scott, G., Roskelley, C., Medrano, E.E., Linskens, M., Rubelj, I., Pereira-Smith, O., et al. (1995). A biomarker that identifies senescent human cells in culture and in aging skin in vivo. Proc. Natl. Acad. Sci. USA 92, 9363–9367.

Dörr, J.R., Yu, Y., Milanovic, M., Beuster, G., Zasada, C., Däbritz, J.H., Lisec, J., Lenze, D., Gerhardt, A., Schleicher, K., et al. (2013). Synthetic lethal metabolic targeting of cellular senescence in cancer therapy. Nature 501, 421–425.

el-Deiry, W.S., Tokino, T., Velculescu, V.E., Levy, D.B., Parsons, R., Trent, J.M., Lin, D., Mercer, W.E., Kinzler, K.W., and Vogelstein, B. (1993). WAF1, a potential mediator of p53 tumor suppression. Cell 75, 817–825.

Elmore, L.W., Di, X., Dumur, C., Holt, S.E., and Gewirtz, D.A. (2005). Evasion of a single-step, chemotherapy-induced senescence in breast cancer cells: implications for treatment response. Clin. Cancer Res. 11, 2637–2643.

Elowitz, M.B., Levine, A.J., Siggia, E.D., and Swain, P.S. (2002). Stochastic gene expression in a single cell. Science 297, 1183–1186.

Ewald, J.A., Desotelle, J.A., Wilding, G., and Jarrard, D.F. (2010). Therapy-induced senescence in cancer. J. Natl. Cancer Inst. 102, 1536–1546.

Fang, L., Igarashi, M., Leung, J., Sugrue, M.M., Lee, S.W., and Aaronson, S.A. (1999). p21Waf1/Cip1/Sdi1 induces permanent growth arrest with markers of replicative senescence in human tumor cells lacking functional p53. Oncogene 18, 2789–2797.

Gewirtz, D.A. (1999). A critical evaluation of the mechanisms of action proposed for the antitumor effects of the anthracycline antibiotics adriamycin and daunorubicin. Biochem. Pharmacol. 57, 727–741.

Greene, R.F., Collins, J.M., Jenkins, J.F., Speyer, J.L., and Myers, C.E. (1983). Plasma pharmacokinetics of adriamycin and adriamycinol: implications for the design of in vitro experiments and treatment protocols. Cancer Res. 43, 3417–3421.

Han, Z., Wei, W., Dunaway, S., Darnowski, J.W., Calabresi, P., Sedivy, J., Hendrickson, E.A., Balan, K.V., Pantazis, P., and Wyche, J.H. (2002). Role of p21 in apoptosis and senescence of human colon cancer cells treated with camptothecin. J. Biol. Chem. 277, 17154–17160.

Haugstetter, A.M., Loddenkemper, C., Lenze, D., Gröne, J., Standfuss, C., Petersen, I., Dörken, B., and Schmitt, C.A. (2010). Cellular senescence predicts treatment outcome in metastasised colorectal cancer. Br. J. Cancer 103, 505–509.

He, G., Siddik, Z.H., Huang, Z., Wang, R., Koomen, J., Kobayashi, R., Khokhar, A.R., and Kuang, J. (2005). Induction of p21 by p53 following DNA damage inhibits both Cdk4 and Cdk2 activities. Oncogene 24, 2929–2943.

Hickson, I., Zhao, Y., Richardson, C.J., Green, S.J., Martin, N.M., Orr, A.I., Reaper, P.M., Jackson, S.P., Curtin, N.J., and Smith, G.C. (2004). Identification and characterization of a novel and specific inhibitor of the ataxia-telangiectasia mutated kinase ATM. Cancer Res. 64, 9152–9159.

Insinga, A., Cicalese, A., Faretta, M., Gallo, B., Albano, L., Ronzoni, S., Furia, L., Viale, A., and Pelicci, P.G. (2013). DNA damage in stem cells activates p21, inhibits p53, and induces symmetric self-renewing divisions. Proc. Natl. Acad. Sci. USA 110, 3931–3936.

Janes, K.A., Albeck, J.G., Gaudet, S., Sorger, P.K., Lauffenburger, D.A., and Yaffe, M.B. (2005). A systems model of signaling identifies a molecular basis set for cytokine-induced apoptosis. Science 310, 1646–1653.

Jaqaman, K., Loerke, D., Mettlen, M., Kuwata, H., Grinstein, S., Schmid, S.L., and Danuser, G. (2008). Robust single-particle tracking in live-cell time-lapse sequences. Nat. Methods 5, 695–702.

Jung, Y.S., Qian, Y., and Chen, X. (2010). Examination of the expanding pathways for the regulation of p21 expression and activity. Cell. Signal. 22, 1003–1012.

Kang, J., Hsu, C.H., Wu, Q., Liu, S., Coster, A.D., Posner, B.A., Altschuler, S.J., and Wu, L.F. (2016). Improving drug discovery with high-content phenotypic screens by systematic selection of reporter cell lines. Nat. Biotechnol. 34, 70–77.

King, C., Diaz, H., Barnard, D., Barda, D., Clawson, D., Blosser, W., Cox, K., Guo, S., and Marshall, M. (2014). Characterization and preclinical development of LY2603618: a selective and potent Chk1 inhibitor. Invest. New Drugs 32, 213–226.

Krenning, L., Feringa, F.M., Shaltiel, I.A., van den Berg, J., and Medema, R.H. (2014). Transient activation of p53 in G2 phase is sufficient to induce senescence. Mol. Cell 55, 59–72.

Kuilman, T., Michaloglou, C., Mooi, W.J., and Peeper, D.S. (2010). The essence of senescence. Genes Dev. 24, 2463–2479.

Kurz, E.U., Douglas, P., and Lees-Miller, S.P. (2004). Doxorubicin activates ATM-dependent phosphorylation of multiple downstream targets in part through the generation of reactive oxygen species. J. Biol. Chem. 279, 53272–53281.

Kwon, J.S., Everetts, N.J., Wang, X., Wang, W., Della Croce, K., Xing, J., and Yao, G. (2017). Controlling Depth of Cellular Quiescence by an Rb-E2F Network Switch. Cell Rep. 20, 3223–3235.

Lanni, J.S., and Jacks, T. (1998). Characterization of the p53-dependent postmitotic checkpoint following spindle disruption. Mol. Cell. Biol. 18, 1055–1064.

Ling, Y.H., el-Naggar, A.K., Priebe, W., and Perez-Soler, R. (1996). Cell cycle-dependent cytotoxicity, G2/M phase arrest, and disruption of p34cdc2/cyclin B1 activity induced by doxorubicin in synchronized P388 cells. Mol. Pharmacol. 49, 832–841.

Ludwig, D., Jones, D.D., and Holling, C.S. (1978). Qualitative-Analysis of Insect Outbreak Systems - Spruce Budworm and Forest. J. Anim. Ecol. 47, 315–332.

Mah, L.J., El-Osta, A., and Karagiannis, T.C. (2010). gammaH2AX: a sensitive molecular marker of DNA damage and repair. Leukemia 24, 679–686.

Maréchal, A., and Zou, L. (2013). DNA damage sensing by the ATM and ATR kinases. Cold Spring Harb. Perspect. Biol. 5. Published online September 1, 2013. https://doi.org/10.1101/cshperspect.a012716.

Nardella, C., Clohessy, J.G., Alimonti, A., and Pandolfi, P.P. (2011). Pro-senescence therapy for cancer treatment. Nat. Rev. Cancer 11, 503–511.

Nishitani, H., Shiomi, Y., Iida, H., Michishita, M., Takami, T., and Tsurimoto, T. (2008). CDK inhibitor p21 is degraded by a proliferating cell nuclear antigen-coupled Cul4-DDB1Cdt2 pathway during S phase and after UV irradiation. J. Biol. Chem. 283, 29045–29052.

O'Connor, M.J. (2015). Targeting the DNA Damage Response in Cancer. Mol. Cell *60*, 547–560.

Overton, K.W., Spencer, S.L., Noderer, W.L., Meyer, T., and Wang, C.L. (2014). Basal p21 controls population heterogeneity in cycling and quiescent cell cycle states. Proc. Natl. Acad. Sci. USA *111*, E4386–E4393.

Paek, A.L., Liu, J.C., Loewer, A., Forrester, W.C., and Lahav, G. (2016). Cell-to-Cell Variation in p53 Dynamics Leads to Fractional Killing. Cell *165*, 631–642.

Passos, J.F., Nelson, G., Wang, C., Richter, T., Simillion, C., Proctor, C.J., Miwa, S., Olijslagers, S., Hallinan, J., Wipat, A., et al. (2010). Feedback between p21 and reactive oxygen production is necessary for cell senescence. Mol. Syst. Biol. *6*, 347.

Potter, A.J., Gollahon, K.A., Palanca, B.J., Harbert, M.J., Choi, Y.M., Moskovitz, A.H., Potter, J.D., and Rabinovitch, P.S. (2002). Flow cytometric analysis of the cell cycle phase specificity of DNA damage induced by radiation, hydrogen peroxide and doxorubicin. Carcinogenesis *23*, 389–401.

Rayess, H., Wang, M.B., and Srivatsan, E.S. (2012). Cellular senescence and tumor suppressor gene p16. Int. J. Cancer *130*, 1715–1725.

Reinhardt, H.C., Hasskamp, P., Schmedding, I., Morandell, S., van Vugt, M.A., Wang, X., Linding, R., Ong, S.E., Weaver, D., Carr, S.A., and Yaffe, M.B. (2010). DNA damage activates a spatially distinct late cytoplasmic cell-cycle checkpoint network controlled by MK2-mediated RNA stabilization. Mol. Cell *40*, 34–49.

Reyes, J., Chen, J.Y., Stewart-Ornstein, J., Karhohs, K.W., Mock, C.S., and Lahav, G. (2018). Fluctuations in p53 Signaling Allow Escape from Cell-Cycle Arrest. Mol. Cell *71*, 581–591.

Roberson, R.S., Kussick, S.J., Vallieres, E., Chen, S.Y., and Wu, D.Y. (2005). Escape from therapy-induced accelerated cellular senescence in p53-null lung cancer cells and in human lung cancers. Cancer Res. *65*, 2795–2803.

Roninson, I.B. (2003). Tumor cell senescence in cancer treatment. Cancer Res. *63*, 2705–2715.

Ruan, S., Okcu, M.F., Ren, J.P., Chiao, P., Andreeff, M., Levin, V., and Zhang, W. (1998). Overexpressed WAF1/Cip1 renders glioblastoma cells resistant to chemotherapy agents 1,3-bis(2-chloroethyl)-1-nitrosourea and cisplatin. Cancer Res. *58*, 1538–1543.

Ryl, T., Kuchen, E.E., Bell, E., Shao, C., Florez, A.F., Monke, G., Gogolin, S., Friedrich, M., Lamprecht, F., Westermann, F., et al. (2017). Cell-Cycle Position of Single MYC-Driven Cancer Cells Dictates Their Susceptibility to a Chemotherapeutic Drug. Cell Syst. *5*, 237–250.

Schmitt, C.A., Fridman, J.S., Yang, M., Lee, S., Baranov, E., Hoffman, R.M., and Lowe, S.W. (2002). A senescence program controlled by p53 and p16INK4a contributes to the outcome of cancer therapy. Cell *109*, 335–346.

Seoane, J., Le, H.V., and Massagué, J. (2002). Myc suppression of the p21(Cip1) Cdk inhibitor influences the outcome of the p53 response to DNA damage. Nature *419*, 729–734.

Shaltiel, I.A., Krenning, L., Bruinsma, W., and Medema, R.H. (2015). The same, only different - DNA damage checkpoints and their reversal throughout the cell cycle. J. Cell Sci. *128*, 607–620.

Shiotani, B., and Zou, L. (2009). Single-stranded DNA orchestrates an ATM-to-ATR switch at DNA breaks. Mol. Cell *33*, 547–558.

Smith, J., Tho, L.M., Xu, N., and Gillespie, D.A. (2010). The ATM-Chk2 and ATR-Chk1 pathways in DNA damage signaling and cancer. Adv. Cancer Res. *108*, 73–112.

Spencer, S.L., Cappell, S.D., Tsai, F.C., Overton, K.W., Wang, C.L., and Meyer, T. (2013). The proliferation-quiescence decision is controlled by a bifurcation in CDK2 activity at mitotic exit. Cell *155*, 369–383.

Starostina, N.G., and Kipreos, E.T. (2012). Multiple degradation pathways regulate versatile CIP/KIP CDK inhibitors. Trends Cell Biol. *22*, 33–41.

Sternberg, S.R. (1983). Biomedical Image-Processing. Computer *16*, 22–34.

Stewart-Ornstein, J., and Lahav, G. (2016). Dynamics of CDKN1A in Single Cells Defined by an Endogenous Fluorescent Tagging Toolkit. Cell Rep. *14*, 1800–1811.

Stoeger, T., Battich, N., Herrmann, M.D., Yakimovich, Y., and Pelkmans, L. (2015). Computer vision for image-based transcriptomics. Methods *85*, 44–53.

Suzuki, K., Kostin, S., Person, V., Elsässer, A., and Schaper, J. (2001). Time course of the apoptotic cascade and effects of caspase inhibitors in adult rat ventricular cardiomyocytes. J. Mol. Cell. Cardiol. *33*, 983–994.

Taylor, W.R., and Stark, G.R. (2001). Regulation of the G2/M transition by p53. Oncogene *20*, 1803–1815.

te Poele, R.H., Okorokov, A.L., Jardine, L., Cummings, J., and Joel, S.P. (2002). DNA damage is able to induce senescence in tumor cells in vitro and in vivo. Cancer Res. *62*, 1876–1883.

Tovar, C., Rosinski, J., Filipovic, Z., Higgins, B., Kolinsky, K., Hilton, H., Zhao, X., Vu, B.T., Qing, W., Packman, K., et al. (2006). Small-molecule MDM2 antagonists reveal aberrant p53 signaling in cancer: implications for therapy. Proc. Natl. Acad. Sci. USA *103*, 1888–1893.

Uetake, Y., and Sluder, G. (2010). Prolonged prometaphase blocks daughter cell proliferation despite normal completion of mitosis. Curr. Biol. *20*, 1666–1671.

Wei, W., Ayad, N.G., Wan, Y., Zhang, G.J., Kirschner, M.W., and Kaelin, W.G., Jr. (2004). Degradation of the SCF component Skp2 in cell-cycle phase G1 by the anaphase-promoting complex. Nature *428*, 194–198.

Xiao, Z., Xue, J., Sowin, T.J., and Zhang, H. (2006). Differential roles of checkpoint kinase 1, checkpoint kinase 2, and mitogen-activated protein kinase-activated protein kinase 2 in mediating DNA damage-induced cell cycle arrest: implications for cancer therapy. Mol. Cancer Ther. *5*, 1935–1943.

Xue, W., Zender, L., Miething, C., Dickins, R.A., Hernando, E., Krizhanovsky, V., Cordon-Cardo, C., and Lowe, S.W. (2007). Senescence and tumour clearance is triggered by p53 restoration in murine liver carcinomas. Nature *445*, 656–660.

Yang, F., Teves, S.S., Kemp, C.J., and Henikoff, S. (2014). Doxorubicin, DNA torsion, and chromatin dynamics. Biochim. Biophys. Acta *1845*, 84–89.

Yang, H.W., Chung, M., Kudo, T., and Meyer, T. (2017). Competing memories of mitogen and p53 signalling control cell-cycle entry. Nature *549*, 404–408.

STAR★METHODS

KEY RESOURCES TABLE

REAGENT or RESOURCE	SOURCE	IDENTIFIER
Antibodies		
Rabbit monoclonal anti-p21	Cell Signaling Technology	Cat# 2947S; RRID: AB_823586
Rabbit monoclonal anti- phospho-Rb (Ser807/811)	Cell Signaling Technology	Cat# 8516S; RRID: AB_11178658
Mouse monoclonal anti-Ki-67	Cell Signaling Technology	Cat# 9449S
Rabbit monoclonal anti- phospho-Histone H2A.X (Ser139)	Cell Signaling Technology	Cat# 9718S; RRID: AB_2118009
Mouse monoclonal anti-p53	Cell Signaling Technology	Cat# 2524S; RRID: AB_331743
Rabbit monoclonal anti-c-Myc	Cell Signaling Technology	Cat# 5605S; RRID: AB_1903938)
Rabbit monoclonal anti-Skp2	Cell Signaling Technology	Cat# 2652T; RRID: AB_11178941
Mouse monoclonal anti-gamma H2A.X (phospho S139)	Abcam	Cat# ab26350; RRID: AB_470861
Goat polyclonal anti- beta Tubulin	Abcam	Cat# ab21057; RRID: AB_727043
Donkey polyclonal anti-Rabbit IgG (H+L) Alexa Fluor 647	Invitrogen	Cat# A-31573; RRID: AB_2536183
Donkey polyclonal anti-Mouse IgG (H+L) Alexa Fluor 647	Invitrogen	Cat# A-31571; RRID: AB_162542
Donkey polyclonal anti-Rabbit IgG (H+L) Alexa Fluor 488	Invitrogen	Cat# A-21206; RRID: AB_141708
Donkey polyclonal anti-Goat IgG (H+L) Alexa Fluor 546	Invitrogen	Cat# A-11056; RRID: AB_142628
Bacterial and Virus Strains		
Biological Samples		N/A
Chemicals, Peptides, and Recombinant Proteins		
Doxorubicin	Sigma-Aldrich	D1515; CAS: 25316-40-9
Nutlin-3a	Sigma-Aldrich	SML0580; CAS: 675576-98-4
KU-55933 ATM kinase inhibitor	Selleck Chemicals	S1092; CAS: 587871-26-9
LY2603618 Chk1 inhibitor	Selleck Chemicals	S2626; CAS: 911222-45-2
Bortezomib 20S proteasome inhibitor	Selleck Chemicals	S1013; CAS: 179324-69-7
Bleomycin	Selleck Chemicals	S1214; CAS: 9041-93-4
Etoposide	Sigma-Aldrich	E1383; CAS: 33419-42-0
Camptothecin	Cayman Chemical	11694; CAS: 7689-03-4
ABT-263	Selleck Chemicals	S1001; CAS: 923564-51-6
Critical Commercial Assays		
Senescence Cells Histochemical Staining Kit	Sigma-Aldrich	CS0030
Experimental Models: Cell Lines		
Human: A549 cells	NCI-60	N/A
Human: HCT116 cells	UCSF Cell Culture Facility	CCLZR253
Human: H460 cells	NCI-60	N/A
Human: A549 pSeg cells	Kang et al., 2016	N/A
Human: A549 p21V cells	This paper	N/A
Oligonucleotides		
ON-TARGET plus Human CDKN1A siRNA – SMART pool	Dharmacon	L-003471-00-0005
CGACUGUGAUGCGCUAAUG		
CCUAAUCCGCCCACAGGAA		
CGUCAGAACCCAUGCGGCA		
AGACCAGCAUGACAGAUUU		

Continued

REAGENT or RESOURCE	SOURCE	IDENTIFIER
ON-TARGET plus Human TP53 (71557) siRNA – SMART pool	Dharmacon	L-003329-00-0005
GAAAUUUGCGUGUGGAGUA		
GUGCAGCUGUGGGUUGAUU		
GCAGUCAGAUCCUAGCGUC		
GGAGAAUGUUUCACCCUUC		
ON-TARGET plus Human MYC (4609) siRNA – SMART pool	Dharmacon	L-003282-02-0005
ACGGAACUCUUGUGCGUAA		
GAACACACAACGUCUUGGA		
AACGUUAGCUUCACCAACA		
CGAUGUUGUUUCUGUGGAA		
Forward primers for the validation of p21-mVenus CCACAT ACGGCTGTTGTGCATT	Integrated DNA Technologies	N/A
Reverse primers for the validation of p21-mVenus TCTCCTT TTCCTCTCTCCCGGA	Integrated DNA Technologies	N/A
p21 gRNA for CRISPR GGCTTCCTGTGGGCGGATTA	Integrated DNA Technologies	N/A
Recombinant DNA		
Plasmid: mVenus-hyg	Stewart-Ornstein and Lahav, 2016	Plasmid 1A
Software and Algorithms		
Code for the p21 dynamics simulation, see Methods S1	This paper	N/A

LEAD CONTACT AND MATERIALS AVAILABILITY

Further information and requests for resources and reagents should be directed to and will be fulfilled by the Lead Contact, Lani Wu (lani.wu@ucsf.edu).

EXPERIMENTAL MODEL AND SUBJECT DETAILS

Cell Culture

A549, HCT116 and H460 cell lines were used in this study. All cell lines are derived from male humans and have wild-type p53 and null p16. All cell lines (including fluorescently tagged A549 clones) were grown in phenol red free RPMI 1640 medium (Thermo Fisher Scientific, #11835055) containing 10% fetal bovine serum, 100 I.U./mL penicillin and 100 ug/mL streptomycin (Corning, #30-002-CI), at $37°C$, 5% CO_2, and 90% humidity.

METHOD DETAILS

Drug Treatment

Doxorubicin (Sigma-Aldrich, D1515) was used to induce senescence at 50 nM (20 nM for H460). Etoposide (Sigma-Aldrich, E1383) was used at 500 nM (125 nM for H460). Camptothecin (Cayman Chemical, 11694) was used at 30 nM (for A549) and 20 nM (for HCT116 and H460). Bleomycin (Selleck Chemicals, S1214) was used at 5 uM (for A549 and H460) and 100 nM (for HCT116). Nutlin-3a (Sigma-Aldrich, SML0580) was used at 10 μM as pretreatment or at indicated concentrations as co-treatment. KU-55933 (Selleck Chemicals, S1092) was used at 10 uM. LY2603618 (Selleck Chemicals, S2626) was used at 5 uM. Bortezomib (Selleck Chemicals, S1013) was used at 40 nM.

Cell Line Construction

We followed the eFlut protocol (Stewart-Ornstein and Lahav, 2016) to construct endogenously Venus-tagged p21 cell lines. Cas9 plasmid containing p21 gRNA sequence (GGCTTCCTGTGGGCGGATTA) and Venus plasmid containing hygromycin B resistance gene were kind gift from Dr. Galit Lahav. In short, we transfected pSeg A549 cell line (which contains H2B-fused CFP in nucleus and mCherry in whole cell) (Kang et al., 2016) with Cas9-p21 gRNA plasmid and Venus dsDNA PCR product using lipofectamine 3000 (Thermo Fisher Scientific, # L3000008). Four days after transfection, hygromycin B was added to the medium at 500 ug/mL, and cells were selected for 9 days. Survival cells were isolated into single cells and expanded into monoclonal cell lines.

Senescence-Associated β-galactosidase Assay

Senescence-associated β-galactosidase activity was detected five days after the induction of senescence using Senescence Cells Histochemical Staining Kit (Sigma-Aldrich, CS0030) following manufacturing protocol in 96-well format.

Immunofluorescence

Cells were fixed with 4% paraformaldehyde for 15 minutes, and then washed three times with PBS followed by permeabilization and blocking with 2% bovine serum albumin protein in 0.1% Triton X-100 (Sigma-Aldrich, 93443) for one hour. Cells were then incubated with primary antibodies at 4°C overnight. The next day, after washing three times with PBS, secondary antibodies and Hoechst (1:2000, Invitrogen, H3570) were applied for 2 hours. Finally, cells were washed with PBS three times before imaging. All antibodies were diluted in PBS with 0.5% bovine serum albumin protein and 0.1% Triton X-100.

siRNA Transfection

ON-TARGET plus Human CDKN1A siRNA – SMART pool (Dharmacon, L-003471-00-0005) was used at 25 nM. ON-TARGET plus Human TP53 (71557) siRNA – SMART pool (Dharmacon, L-003329-00-0005) was used at 25 nM. ON-TARGET plus Human MYC (4609) siRNA – SMART pool (Dharmacon, L-003282-02-0005) was used at 25 nM. Lipofectamine 3000 (Invitrogen, L3000008) was used following the manufacturer's protocol for transfecting cells with siRNA.

EdU Assay

Cells were treated with 0.1% DMSO or 50 nM doxorubicin together with EdU for 24 hours. Images were taken every 20 minutes to record p21 dynamics during this 24-hour period. Cells were then fixed, permeabilized, and stained for β-tubulin as described in "Immunofluorescence" section. After applying secondary antibodies, EdU click reaction was performed by incubating cells with mixture solution containing 1 mM $CuSO_4$, 5 μM sulfo-Cy5 azide, 0.1 M sodium (L) ascorbate in PBS for 30 minutes. Cells were washed three times before imaging.

Image Acquisition

Cells were plated on glass-based 96-well plate (Thermo Scientific, 164588). Images were acquired using a Nikon TE-2000 E2 epi-fluorescence microscope equipped with integrated Perfect-Focus (PFS), Nikon Plan Apochromat Lambda 10x objective lens, Nikon Plan Apochromat VC 20x DIC N2 objective lens, and Zyla 5.5 sCMOS camera (Andor Technology). Time-lapse imaging was performed with an on-stage incubator equipped with temperature and CO_2 controllers (Okolab).

QUANTIFICATION AND STATISTICAL ANALYSIS

Image Analysis and Cell Tracking

Illumination correction was performed by first estimating pixel-wise mean and standard deviation (std) using all images (Stoeger et al., 2015). The 2-D mean and std matrices we obtained were smoothed using a low-pass Gaussian kernel before being used to convert image intensities, pixel-wise, to z-scores. These resulting "z-score matrices" were rescaled to obtain "flattened" images by multiplying the z-score matrices by a reference std (= mean value of the 2-D std matrix) and adding a reference mean value (= mean values of the 2-D mean matrix). The final corrected images were obtained by subtracting background from the flattened images using rolling ball algorithm (Sternberg, 1983).

Cell segmentation was performed using MATLAB functions developed in-house. Nuclei were segmented using H2B intensity (live-cell) or Hoechst intensity (fixed assays) and then refined by marker-based watershed. Nuclear masks were used as "seeds" for watershed to segment cellular regions (mCherry for live-cell and β-tubulin for fixed assays). As some cells have more than one nucleus, a support vector machine classifier was trained to accept/reject each watershed boundary to be a true cellular boundary.

Cell tracking was mainly based on a previously described linear assignment framework (Jaqaman et al., 2008). Track segments were established by linking cells to the closest cells in the next frame. The "distance" was defined as a weighted sum of cell centroid distance and total mCherry intensity ratio between candidate cell pairs. To compile track segments into complete tracks, we used integer programming (Bise et al., 2011) to incorporate different events such as mitosis or detection failure. Track quality was evaluated by length, number of missing frames, and ratio change of total H2B and mCherry intensity between adjacent frames. Erroneous tracks were removed from downstream analysis.

In Silico Cell-Cycle Inference

Cell-cycle inference consists of three steps (detailed below). First, we identified cell division events from time-lapse movies. Second, S phase was identified as the time period when p21 intensity is undetectable. Then, G1 and G2 phases were assigned according to the time order relative to cell division and S phase.

To detect cell division events, we made use of two properties: (1) total cellular mCherry intensity drops by half after division and (2) average cellular mCherry intensity increases dramatically during mitosis. Therefore, we computed the ratio of total cellular mCherry between adjacent frames and average cellular mCherry intensity at each time point. Cell-division events were called if both values exceeded preset thresholds.

p21 is degraded during S phase (Starostina and Kipreos, 2012). We inferred that cells were in S phase when p21 intensity was undetectable. Since p21 is almost exclusively expressed in the nucleus in our study, we used the average cytoplasmic p21 intensity as an estimate of background intensity. Specifically, we computed the ratio of p21 intensity between nuclear and cytoplasmic region, and S phase was assigned when this value was close to one.

Quantification of EdU Intensity
After cell segmentation, EdU signal was quantified by the total intensity in the nuclear region of each individual cell. To determine whether a cell ever incorporated EdU during an experiment, we first established a distribution of EdU background intensity by measuring EdU intensity in the cytoplasmic region. The 99% quantile of the EdU background intensity distribution was used as a threshold to determine whether a cell had synthesized DNA (EdU$^+$ cells).

Definition of p21 Induction
We noted that untreated cells typically display a low level of basal p21 expression. In a drug-treated cell, we defined that p21 is induced when its intensity level exceeds the 95% quantile of basal p21 expression levels in an untreated population. The response time of p21 induction is the first time point when p21 is induced (by drug).

Definition of Dwell Phase
Cell-cycle arrest usually implies that a cell stays exclusively in a particular cell-cycle phase (longer than it normally does). However, from our inferred cell-cycle phases, we observed that individual cells indeed spent significantly longer, but not necessarily their entire time, in a particular cell-cycle phase during drug pulse. To avoid potential confusion of terminology, we defined "dwell phase" as the longest (and significantly longer than normal) cell-cycle phase that a cell stayed in during drug pulse. Specifically, we first calculated the longest cell-cycle phase that an individual cell stayed in during drug pulse. To stringently compare the duration of this putative dwell phase to typical lengths of each cell-cycle phase under normal conditions, we collected maximal lengths that our collection of cells had for each cell-cycle phase before treatment (-24 to 0 hour). Then, we set thresholds to be 3 standard deviations (robustly estimated by $1.4826 \times$ median absolute deviation) higher than median for each cell-cycle phase. Cells with dwell phases shorter than the corresponding thresholds were excluded from the analysis ($< 10\%$).

Comparison of p21 Expression during Dwell Phase between Cellular Subpopulations
For each cell, the maximal levels of p21 expression during its dwell phase (p21$_{max}$) was computed. Cells were then grouped into three subpopulations based on dwell phase and cell fate: (1) G1 dwell phase with senescence fate, (2) G1 dwell phase with proliferation fate, and (3) S/G2 dwell phase with senescence fate. A one-sided rank-sum test was used to assess the significance of differences in p21$_{max}$ between these three subpopulations.

Inference of Cell-Cycle Phase using Hoechst Intensity
For fixed-cell assays, we used Hoechst intensity to infer cell-cycle phases. Hoechst intensity typically shows a bimodal distribution with lower mode at G1, higher mode at G2. Therefore, we applied a Gaussian mixture model to infer cell-cycle phases of individual cells based on Hoechst intensity. Specifically, we first quantified total Hoechst intensity in nuclear regions of each individual cell. Then, we fitted a Gaussian mixture model with three components (accounting for cells in S phase) to the distribution of Hoechst intensity. The boundaries at G1/S and S/G2 were chosen to be 3 standard deviations above G1 mode and below G2 mode, respectively.

Quantification of DNA-Damage Sensitivity (Δp21/$\Delta\gamma$H2A.X)
We quantified damage sensitivity as the increased amount of p21 level (Δp21, compared to p21 levels under untreated conditions) in response to the increased amount of DNA damage ($\Delta\gamma$H2A.X, compared to γH2A.X levels under untreated conditions). Specifically, we fit a linear regression model (p21 versus γH2A.X) for each given cell-cycle phase across all indicated time points (0 hour is untreated condition). The sensitivity was measured by the slope (Δp21/$\Delta\gamma$H2A.X) of the linear regression model.

Definition of Ki-67$^+$ Cells
Ki-67 intensity shows a bimodal distribution at day 5 after a one-day pulsed doxorubicin treatment. We fit a Gaussian mixture model with two components (high and low-expression) to the data. The Ki-67 threshold was defined to be the minimal intensity value for which the posterior probability of belonging to the high-expression group is larger than 0.5.

Mathematical Model of p21 Dynamics
The goal of our mathematical model was to provide a framework for understanding the emergence of different patterns of p21 dynamics. Our data suggested bistable states of p21 expression levels after drug treatment: p21^{high} is associated with senescence fate and p21^{low} is associated with proliferation fate. To model the observed p21 dynamics in drug-treated conditions, we extended a previously developed mathematical model that accounts for p21 bistability (with CDK2) in an unperturbed condition

(Overton et al., 2014). Specifically, we added DNA-damage-dependent p21 generation and p21 positive feedback (Passos et al., 2010) to the original model. The p21 dynamics was then described by the following differential equation:

$$\frac{dp21}{dt} = c^* damage(t) + f(p21) + k_{gen,p21} - k_2 g(CDK2_{active})p21 - b_{deg,p21}p21 + noise$$

$$g(CDK2_{active}) = \frac{CDK2_{active}^{n_2}}{K_{M2}^{n_2} + CDK2_{active}^{n_2}}$$

The cell-cycle-dependent function $damage(t)$ was obtained from our measured γH2A.X levels (Figure S5A). The positive feedback function $f(p21)$ was described by:

$$f(p21) = r^* p21^2 \left(1 - \frac{p21}{K}\right)$$

$CDK2_{active}$ was assumed to depend on instantaneous p21 levels (Reyes et al., 2018):

$$CDK2_{active} = \frac{k_1 GF}{\frac{k_3 p21^{n_1}}{K_{M1}^{n_1} + p21^{n_1}} + b_{deg,CDK2}}$$

which is the steady state of $CDK2_{active}$ described in the original model (Overton et al., 2014). Lastly, we added Gaussian noise (noise) with 1% coefficient of variation during the simulation to describe stochastic gene expression (Elowitz et al., 2002). For simplicity, cell-cycle phases were fixed (i.e., entry phase = dwell phase) for each cell during the simulation.

We searched for a parameter set that could recapitulate our observed patterns of p21 dynamics (Table S1). We first adjusted parameters used in the original model so that p21 levels of G1 cells in our model recaptured the bistability under unperturbed conditions ($damage(t) = 0$). (The adjusted parameters were around the same order of magnitude as used in the original model.) We then set parameters related to damage sensitivity (c), p21 positive feedback (r, K) and CDK2-dependent p21 degradation $g(CDK2_{active})$ to reflect differences between G1 and S/G2 cellular populations (Figure 4; Table S1). The p21 dynamics of 1000 single cells were simulated using Euler's method implemented with customized MATLAB script (Methods S1).

We note that other mathematical models can also recapitulate the three patterns of p21 dynamics (e.g., the "insect outbreak" model (Ludwig et al., 1978)). The key feature was the saddle-node bifurcation induced by increasing DNA damage (Figure 5A, right).

DATA AND CODE AVAILABILITY

Code for the model simulation of p21 dynamics is included in Methods S1.
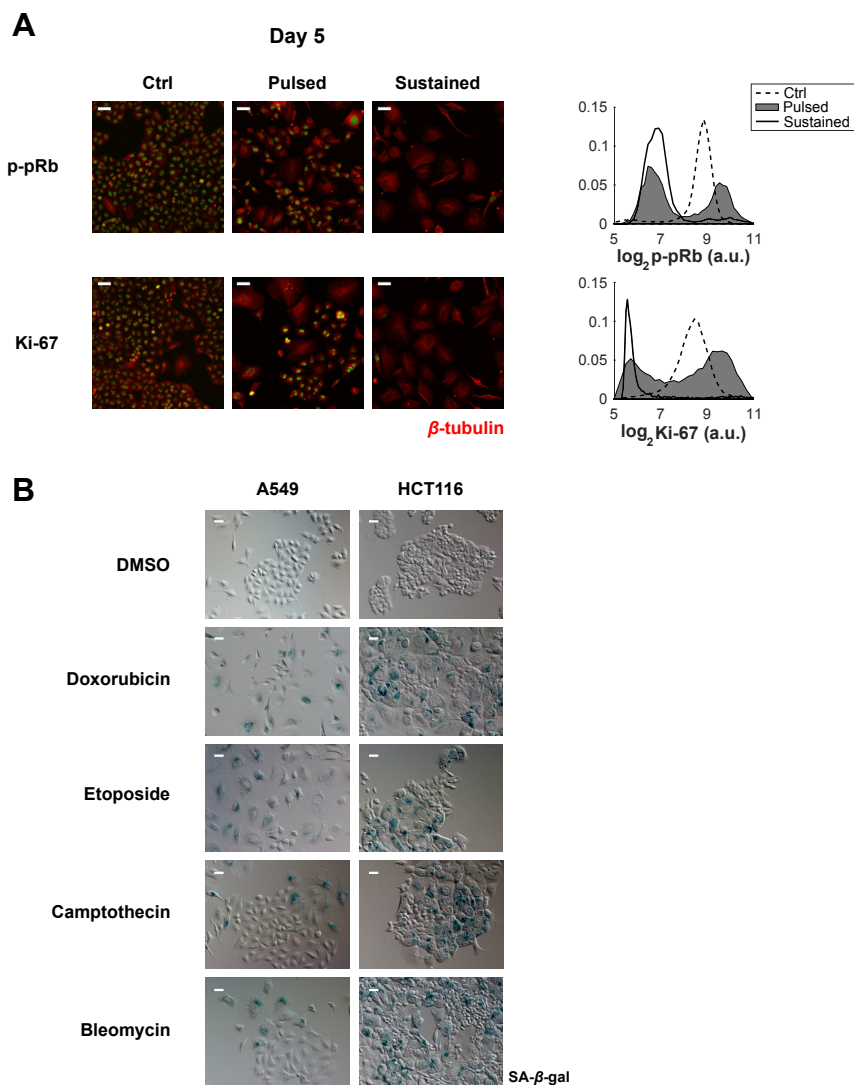
Supplemental Figures

Figure S1. 1-Day Pulsed Drug Treatment Leads to Mixed Proliferation and Senescence Fates across Multiple Cell Lines and Drugs, Related to Figure 1

(A) Left: example images of A549 cells stained with phospho-pRb or Ki-67 at day 5 after no treatment (Ctrl), pulsed (Pulsed), or continuous (Sustained) doxorubicin treatment at 50 nM. Right: distributions of each marker quantified by immunofluorescence at day 5 after indicated treatment schemes. At least 3241 cells were examined for each marker under each treatment condition. Green channel: markers. Red channel: β-tubulin. Scale bar: 20 μm.

(B) Images of A549 and HCT116 cells stained with senescence-associated β-galactosidase at day 5 after pulsed treatment of doxorubicin (50 nM), etoposide (500 nM), camptothecin (A549: 30 nM, HCT116: 20 nM), and bleomycin (A549: 5 μM, HCT116: 100 nM). Scale bar: 20 μm.
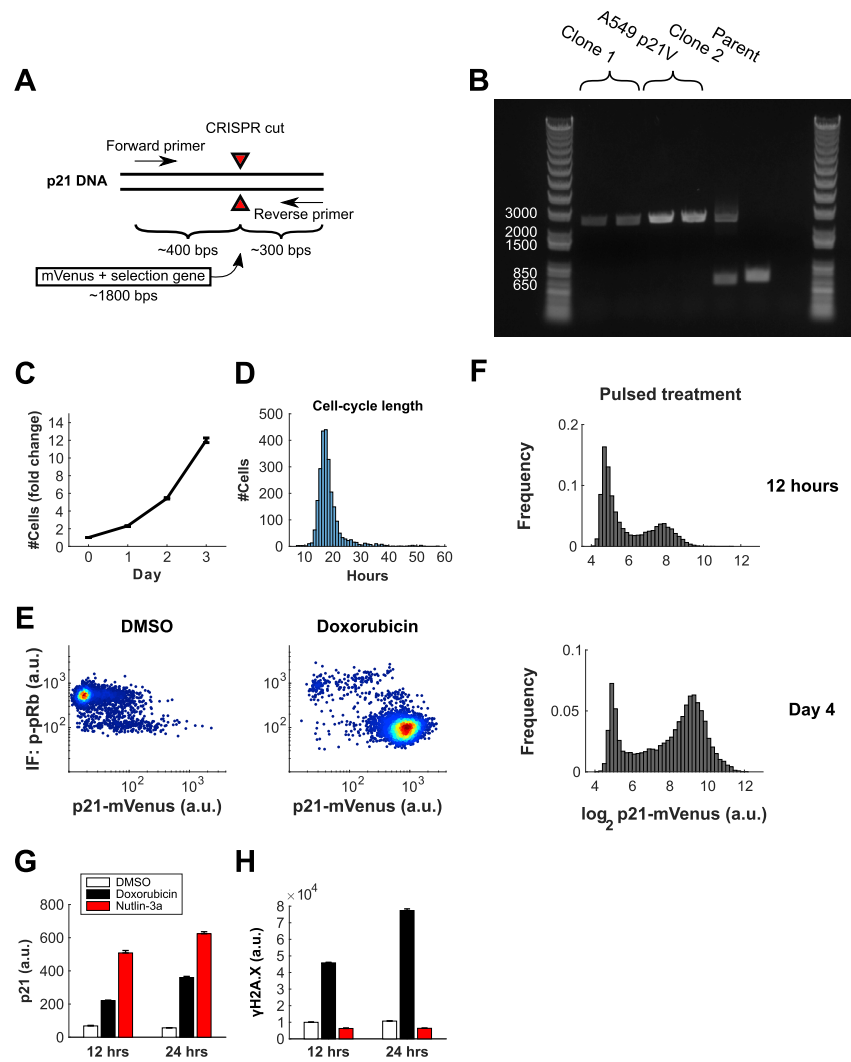
Figure S2. Validation of p21 Live-Cell Reporter Cell Lines, Related to Figure 2

(A) PCR design. Forward and reverse primers were chosen to be ~400 bps upstream and ~300 bps downstream of the CRISPR cutting site (red triangles). The insertion sequence (mVenus + antibiotics resistance gene) is ~1800 bps. Therefore, the expected PCR product of a successful insertion is ~2500 bps.

(B) Gel electrophoresis of PCR products of different clones. Clone 1 and A549 p21V (used in this study) are tagged with mVenus at both alleles. Clone 2 was tagged at only one allele. Parent: A549 cell line.

(C) Fold change of cell number in unperturbed condition. A549 p21V cells were imaged every day. Cell numbers were obtained by image segmentation. Data are represented as mean ± SEM.

(D) Histogram of cell-cycle lengths in unperturbed condition. Cell-cycle lengths of each individual A549 p21V cells were obtained from cell tracking.

(E) Density scatterplots of immunofluorescence of phospho-pRb versus p21-mVenus in single cells under DMSO (left) or after 5 days of 50 nM doxorubicin (right) treatments. At least 3500 cells were quantified under each condition.

(F) Histograms of p21-mVenus expression (top) after 12 hours of 50 nM doxorubicin treatment and (bottom) 4 days after a one-day pulsed doxorubicin (50 nM) treatment. At least 15,000 cells were quantified at each time point.

(G and H) p21 (G) and γH2A.X (H) levels at 12 and 24 hours under DMSO (unperturbed), doxorubicin or nutlin-3a conditions. A549 p21V cells were treated with DMSO, 50 nM doxorubicin or 10 μM nutlin-3a, and then fixed and stained for γH2A.X at 12 and 24 hours. p21 levels were measured by average mVenus intensity in the nuclear region. γH2A.X were measured by total immunofluorescent intensity in the nuclear region. Three replicate experiments were performed for each condition at each time point. More than 900 cells were quantified in each replicate experiment. Data are represented as mean ± SEM.
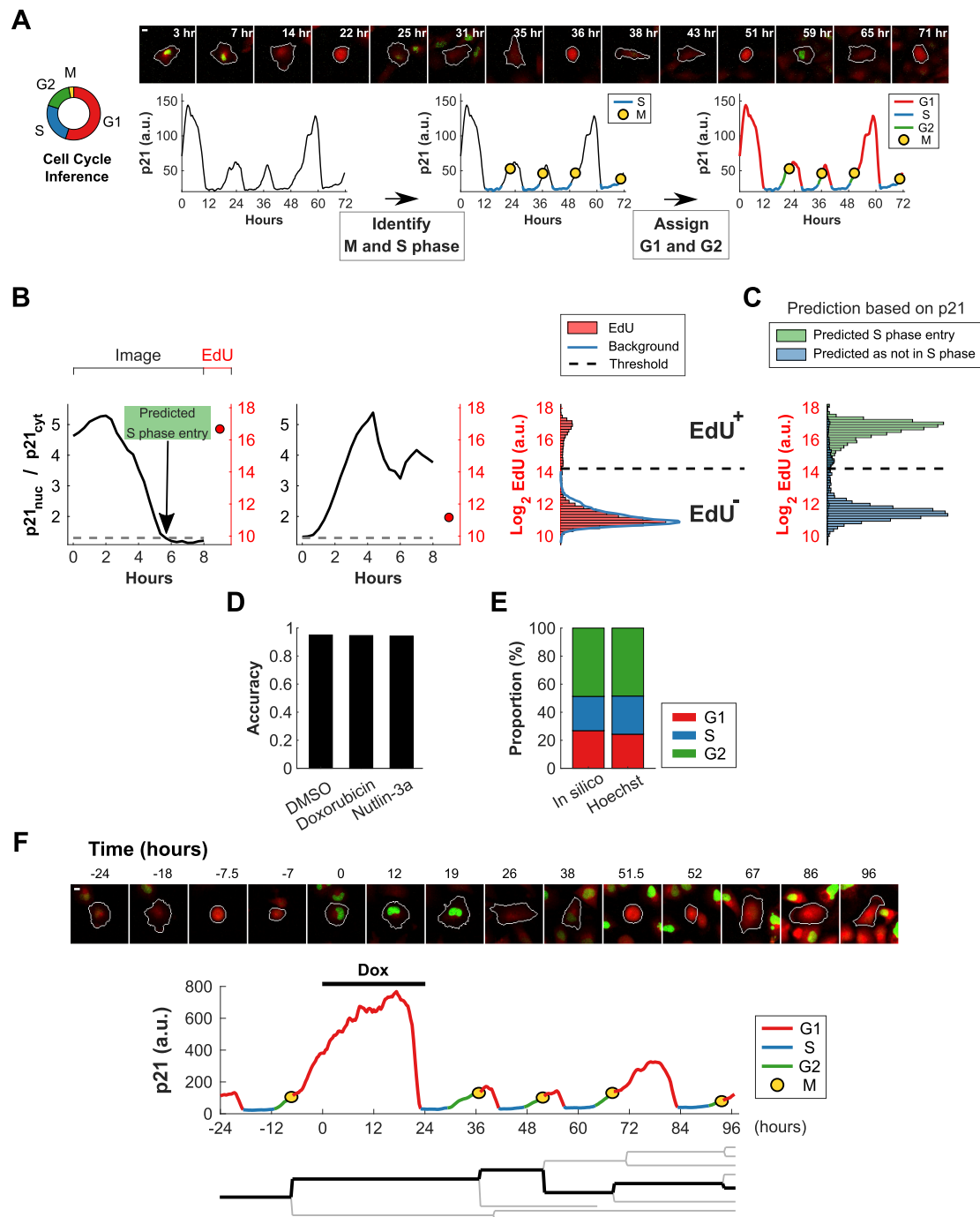
Figure S3. *In Silico* Cell-Cycle Detection Links p21 and Cell-Cycle Dynamics to Cell Fate, Related to Figure 3

(A) Illustration of cell-cycle inference. Images and p21 dynamics of an example cell imaged every 20 minutes for 72 hours under untreated condition are shown to illustrate our approach to infer cell-cycle phases. The indicated time points are approximated for clarity. Green channel: p21. Red channel: mCherry. Scale bar: 10 μm.

(B) Overview of the experiment to validate our *in silico* cell-cycle detection. A549 p21V cells were treated with DMSO (control), 50 nM doxorubicin, or 10 μM nutlin-3a, and imaged every 20 minutes for 8 hours. Cells were then incubated with 10 μM EdU for 15 minutes, followed by fixation and EdU detection. Left and middle: two examples of p21 dynamics with associated final EdU intensity (red circles in left two panels) of single cells from DMSO treatment are shown. A cell was predicted to be in S phase if its p21 intensity was undetectable. Since p21 is almost exclusively expressed in the nucleus for our cells, S phase was predicted when nuclear p21 intensity ($p21_{nuc}$) was close to cytoplasmic intensity ($p21_{cyt}$). Here, 1.3 was empirically chosen as the threshold (gray dashed lines). Right: histogram of EdU intensity of cells under DMSO treatment (red). Imaging background (Background, blue curve) was estimated by average EdU intensity in

(legend continued on next page)

cytoplasmic regions. The threshold of EdU$^+$ was set to be mean plus 6 standard deviations of the background distribution (black dashed line). EdU$^+$ and EdU$^-$ serve as the ground truth for our S-phase prediction.

(C) Histograms of EdU intensity of cells predicted to be in (green) or not in (blue) S phase at the end of imaging based on p21 dynamics. We observed that cells predicted to be in S phase were enriched in the EdU$^+$ region, and vice versa.

(D) Accuracy of S-phase prediction under DMSO, doxorubicin and nutlin-3a treatment. For clarity, we defined (non-)S-phase cells to be cells that were predicted (not) to be in S phase at the end of the experiment based on p21 dynamics. Accuracy is the percentage of predicted S-phase cells that were also EdU$^+$, and non-S-phase cells that were also EdU$^-$. At least 6000 cells were quantified in each condition.

(E) Cell-cycle distribution inferred by our approach (*in silico*) or Hoechst intensity after 12 hours of 50 nM doxorubicin treatment.

(F) Images (top), p21 dynamics (middle) and lineage (bottom) of an example A549 p21V cell imaged every 20 minutes starting 24 hours before a one-day pulsed doxorubicin treatment. p21 dynamics was colored by inferred cell-cycle phases. Green channel: p21. Red channel: mCherry. Scale bar: 10 μm. Dox: doxorubicin.
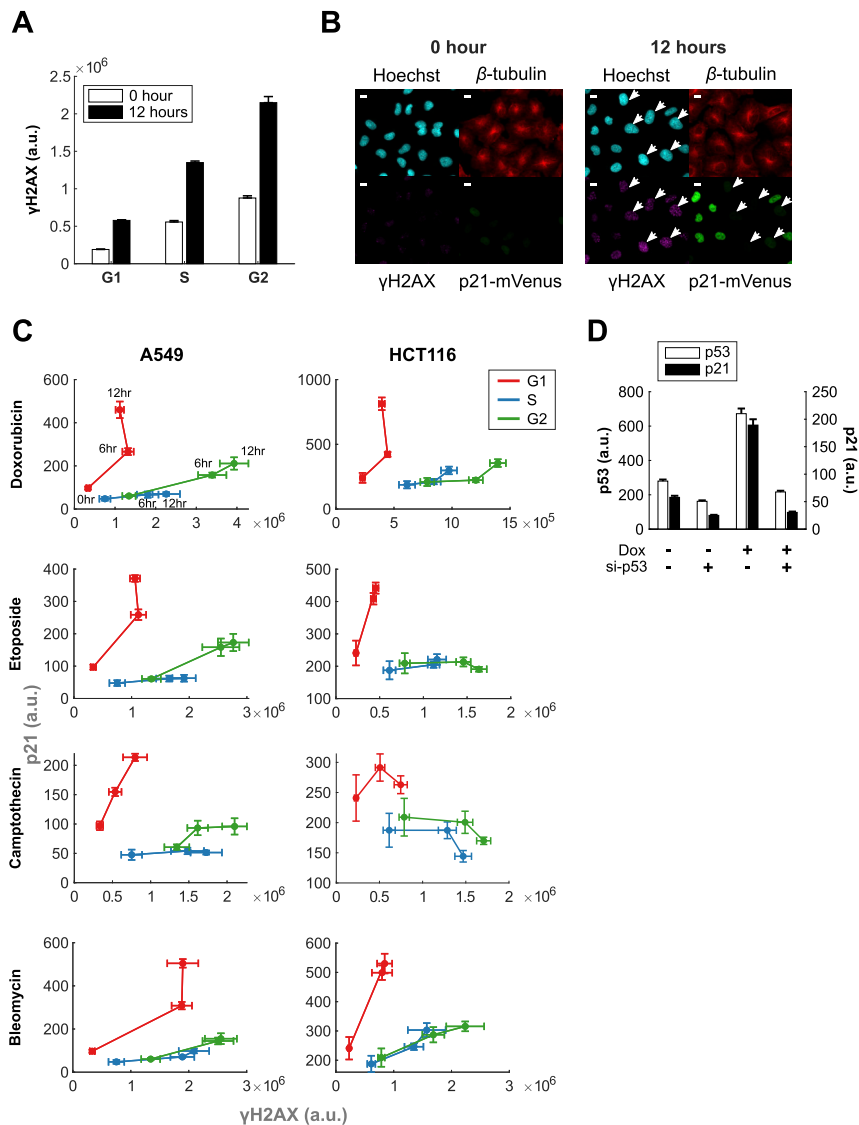
Figure S4. Regulatory Mechanisms of Cell-Cycle-Dependent p21 Expression, Related to Figure 4

(A) Quantification of DNA damage (γH2A.X levels) in each cell-cycle phase at 0 hour and after 12 hours of 50 nM doxorubicin treatment. Data are represented as mean ± SEM.

(B) Sample images of cells at 0 hour (left) and after 12 hours of doxorubicin treatment (right). Arrows indicate cells with high DNA damage (γH2A.X levels) yet low p21 expression. The same intensity scale was used for both two time points. Scale bar: 10 μm.

(C) Time course of p21 versus DNA damage (0, 6 and 12 hours), grouped by cell-cycle phases in A549 p21V and HCT116 cell lines treated with doxorubicin (50 nM), etoposide (500 nM), camptothecin (A549: 30 nM, HCT116: 20 nM), and bleomycin (A549: 5 μM, HCT116: 100 nM). Six replicate experiments were performed for each treatment condition. At least 195 cells were quantified for each cell-cycle phase in each replicate experiment. Data are represented as mean ± SEM.

(D) The effect of p53 knockdown on p21 expression. A549 p21V cells were treated by 25 nM siRNA targeting p53 (si-p53 +) or non-targeting siRNA (si-p53 -) under 50 nM doxorubicin (Dox +) or untreated (Dox -) conditions as indicated. Cells were fixed after 12 hours of treatment, stained for p53 and imaged. Population-averaged p53 immunofluorescent intensity (left axis) and p21-mVenus levels (right axis) are shown. Six replicate experiments were performed for each treatment condition. At least 1675 cells were quantified in each replicate experiment. Data are represented as mean ± SEM.
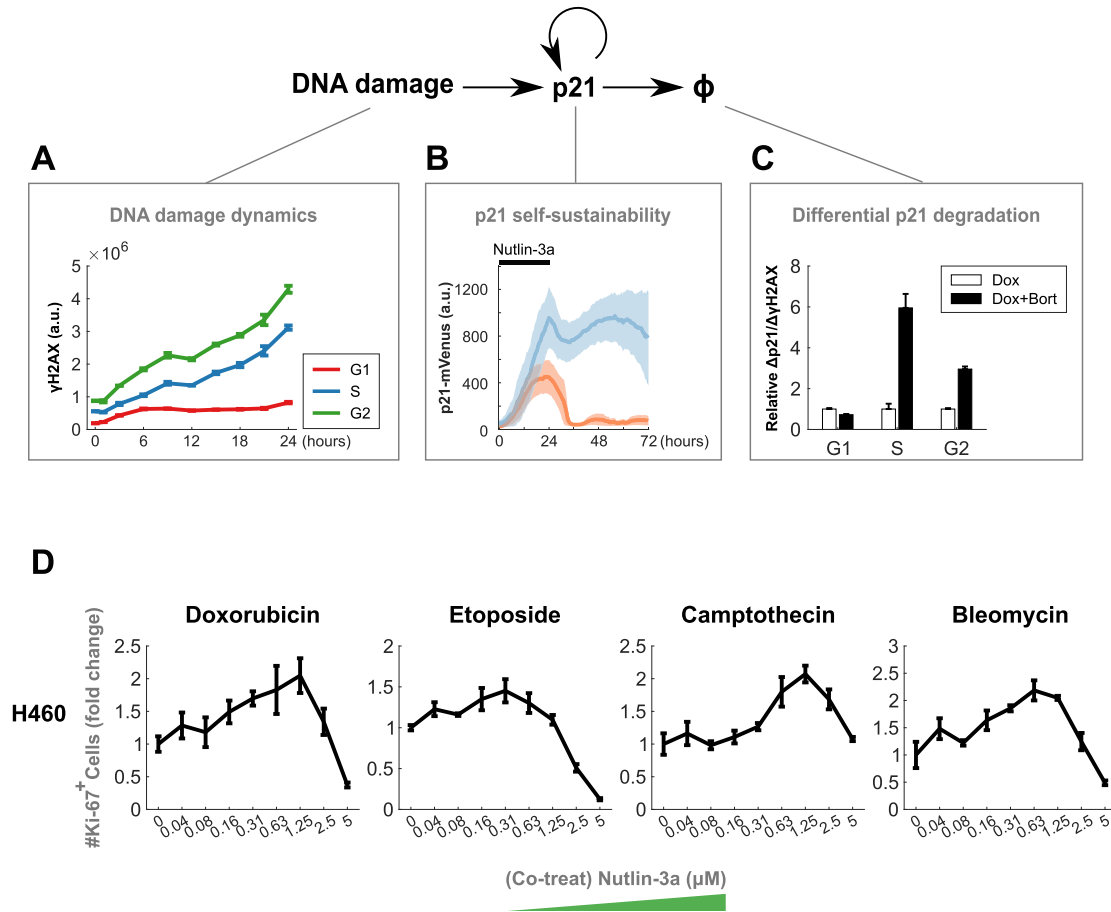
Figure S5. Mathematical Model of p21 Dynamics, Related to Figure 5

(A-C) Data used to constrain the model of p21 dynamics. (A) DNA damage profiles were fit to the measured γH2A.X levels. (B) Nutlin-3a treatment suggested p21 self-sustainability. (C) p21 degradation was cell-cycle dependent (duplication of Figure 4E).

(D) p21 "Goldilocks zone" across multiple chemotherapeutic agents in H460. The experiment was conducted as Figure 5D. Drug concentrations: 20 nM doxorubicin, 125 nM etoposide, 20 nM camptothecin, and 5 μM bleomycin. Six replicate experiments were performed for each condition. Data were normalized to drug-only (0 μM nutlin-3a) treatment, and are represented as mean ± SEM.
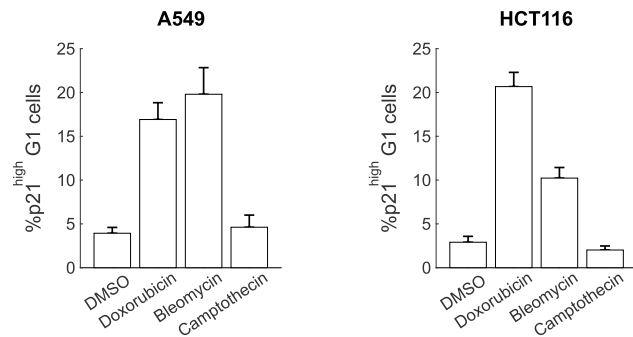
Figure S6. Effects of Chemotherapeutic Agents on G1 Arrest, Related to Figure 6

Cells that activate the G1/S checkpoint are expected to express high levels of p21 and arrest in G1. Thus, we quantified the percentage of G1 cells with p21^{high} expression in either A549 p21V or HCT116 populations after 12-hour treatment with different chemotherapeutic agents. Six replicate experiments were performed and at least 1500 cells were quantified for each treatment condition. Data are represented as mean ± SEM.